

Experimental evidence of analogue Hawking radiation from ultrashort laser pulse filaments

This content has been downloaded from IOPscience. Please scroll down to see the full text.

2011 New J. Phys. 13 085005

(<http://iopscience.iop.org/1367-2630/13/8/085005>)

View [the table of contents for this issue](#), or go to the [journal homepage](#) for more

Download details:

IP Address: 130.209.6.41

This content was downloaded on 03/11/2015 at 09:31

Please note that [terms and conditions apply](#).

Experimental evidence of analogue Hawking radiation from ultrashort laser pulse filaments

E Rubino¹, F Belgiorno², S L Cacciatori^{1,3}, M Clerici^{1,4},
V Gorini^{1,3}, G Ortenzi⁵, L Rizzi¹, V G Sala¹, M Kolesik⁶
and D Faccio^{1,7,8}

¹ Dipartimento di Fisica e Matematica, Università dell'Insubria,
Via Valleggio 11, IT-22100 Como, Italy

² Dipartimento di Fisica, Università degli Studi di Milano, Via Celoria 16,
IT-20133 Milano, Italy

³ INFN Sezione di Milano, via Celoria 16, IT-20133 Milano, Italy

⁴ INRS-EMT, Université du Québec, Varennes, QC, J3X 1S2, Canada

⁵ Dipartimento di Matematica e Applicazioni, Università di Milano-Bicocca,
Via Cozzi 53, IT-20125 Milano, Italy

⁶ College of Optical Sciences, University of Arizona, Tucson, AZ 85721, USA

⁷ School of Engineering and Physical Sciences, SUPA, Heriot-Watt University,
Edinburgh EH14 4AS, UK

E-mail: d.faccio@hw.ac.uk

New Journal of Physics **13** (2011) 085005 (33pp)

Received 17 February 2011

Published 9 August 2011

Online at <http://www.njp.org/>

doi:10.1088/1367-2630/13/8/085005

Abstract. Curved space-times and, in particular, event horizons of astrophysical black holes are expected to excite the quantum vacuum and give rise to an emission of quanta known as Hawking radiation. Remarkably, many physical systems may be considered analogous to black holes and as such hold promise for the detection of Hawking radiation. In particular, recent progress in the field of transformation optics, i.e. the description of optical systems in terms of curved space-time geometries, has led to a detailed description of methods for generating, via superluminal dielectrics, a blocking horizon for photons. Our measurements highlight the emission of photons from a moving refractive index perturbation induced by a laser pulse that is in quantitative agreement with the Hawking model. This opens an intriguing and readily accessible observation window into quantum field theory in curved space-time geometries.

⁸ Author to whom any correspondence should be addressed.

Contents

1. General overview	2
2. Introduction	2
3. Ultrashort laser pulse filamentation	4
3.1. Spontaneous filaments	4
3.2. Bessel filaments	6
4. Propagation equations and the creation of horizons using laser pulses	7
5. The metric and horizon condition	9
6. A comment on the horizon condition	10
7. Stimulated Hawking emission (SHE) and thermality: numerical simulations	12
8. Photon emission angular distribution	17
9. Horizon geometries	20
10. Experimental layout	22
11. Experimental evidence for analogue Hawking radiation	26
12. Concluding remarks	30
Acknowledgments	31
References	31

1. General overview

In this work, we present experimental evidence of a novel photon emission process that finds a detailed description in terms of a mechanism analogous to that of black hole evaporation, also known as Hawking radiation. The experiments are performed in an analogue system, i.e. in an Earth-based laboratory layout that uses intense laser pulses to induce an effective space–time geometry that mimics an event horizon. Part of the experimental results have been published in [1]. Here we add further experimental data and discuss in detail the salient features of the analogue system, in an attempt to address some concerns that have been expressed and to provide the reader with the elements necessary in order to understand the underlying details of the model and experiments.

The paper is organized as a general introduction for the non-specialist with an overview of the theoretically predicted features of the analogue Hawking radiation, followed by a detailed description of the experimental layout and the various competing effects that may occur. We finally present experimental evidence of analogue Hawking radiation and conclude with an outlook on some open questions and challenges.

2. Introduction

One of the most fascinating aspects of laser physics and optics in general is the ability to reproduce, even though to a limited extent, many features of the physics of completely different systems. Extraordinary examples in this sense are semiconductor physics reproduced in photonic crystals and quantum behaviour of electrons in periodic potentials reproduced in periodic optical waveguides. These analogies also imply that the behaviour of light may be

understood or reinterpreted using the tools and the physics developed in very different regimes such as, referring to the two examples above, semiconductor or electron physics. This cross-fertilization between extremely diverse areas of physics, on the one hand, underlines a certain universality in the behaviour of apparently complex systems and, on the other hand, offers novel insights that often lead to significant and new discoveries. Here, we deal with the so-called transformation optics [2].

The underlying idea is that the refractive index of a given medium in which light is propagating acts as a ‘transformation medium’, i.e. it ‘transforms’ the Euclidean space–time in which light rays propagate into some other effective curved space–time. The result is that the light paths followed by the rays appear to be bent and this is a consequence of the effective space–time curvature induced by the medium. As a consequence of this, it is possible to apply the mathematical tools developed in general relativity in order to give a precise and efficient description of light propagation in media with varying refractive indices. A very simple example of this is the optical mirage, which also finds a precise mathematical description in terms of Fermat’s principle and which may therefore be considered as a precursor of transformation optics. A more complicated example is the ‘invisibility cloak’, i.e. a meta-material designed to create a spatial curvature such that light rays propagate around objects that therefore remain hidden from an external observer [3, 4]. Most applications of transformation optics refer to purely spatial or purely temporal transformations (see e.g. [5, 6]). However, the full implications of the analogy with general relativity are evidenced when the full space–time description is investigated.

A first observation is that propagation of light rays inside a medium, in which a dielectric or refractive index perturbation travels, can be described in terms of an effective metric for which the light ray paths are the null geodesics [7–11]. This is in analogy with the description of light rays in the presence of a metric induced by a gravitational body. Therefore, certain properties of the electromagnetic field in the presence of a dielectric perturbation may be described using the tools of general relativity. For example, light ray trajectories may be computed as geodesics within the given metric rather than as the result of Maxwell equations. Notably, this feature also applies to the quantized electromagnetic field. In other words, there are certain, fundamental aspects of quantum field theory in the presence of curved space–times [12] that may be investigated using transformation optics [2, 11, 13].

According to a milestone prediction in this sense, astrophysical black holes, far from being truly black, evaporate, i.e. they emit particles and photons with a blackbody spectrum known as Hawking radiation [14, 15]. It is now widely accepted that Hawking radiation does not actually require a gravitational mass but rather the essential ingredients are a quantum field, e.g. density perturbations in a fluid or the electromagnetic field and an event horizon associated with a curved space–time metric that blocks the quanta of this field, namely phonons or photons [11, 16].

This was explicitly pointed out for the first time by Unruh [16] who proposed an acoustic analogue in order to probe the existence of Hawking radiation in the laboratory. Indeed such radiation has little hope of being detected in the vicinity of astrophysical black holes due to its extremely low temperatures (of the order of 10 nK for a solar-mass black hole). Many proposals have since been put forth, mostly based on analogue Hawking emission in the form of phonons in fluids or Bose–Einstein condensates (BEC) or of photons from moving dielectrics. One of the main difficulties associated with these proposals is, again, the still very low Hawking temperatures predicted by theory. This difficulty could be overcome by resorting

to an indirect verification of Hawking phonon emission in BECs by measuring an increase in the phonon correlation distribution [17, 18]. A more direct approach, based on the idea of transformation optics, was proposed by Philbin *et al* [9], who suggested the use of an intense optical soliton pulse propagating in a dielectric fibre. The soliton intensity is sufficient to induce a refractive index perturbation in the fibre medium, which in turn acts as a space–time curvature of the metric as seen by the quantum electromagnetic vacuum. Due to material dispersion, the dielectric perturbation will become superluminal in the sense that it will move faster than the *phase* velocity of sufficiently blue-shifted wavelengths. The relevance of this condition to the phase velocity for the spontaneous generation of photons from a moving boundary was also pointed out recently by Guerreiro *et al* [19]. The important point is that in this scenario, theoretical predictions suggest extremely high Hawking temperatures in the range of thousands of kelvins and many orders of magnitude higher than that in any other physical system proposed so far. Crucial features of this model are the following [9]:

- (i) the intensity of the laser pulse, because more intense pulses will induce higher dielectric perturbation values and possibly a more efficient photon production;
- (ii) the velocity of the laser pulse, which can be used, in combination with material dispersion, to tune the spectrum of the emitted Hawking photons;
- (iii) the duration or steepness of the laser pulses, which is directly related to the Hawking temperature.

It is therefore essential to control all three of these parameters. Moreover, a delicate issue from an experimental point of view is the ability to identify the electromagnetic radiation associated with the input laser pulse, which may, due to various nonlinear effects, transform dramatically and cover more than an octave in the output spectrum, thus possibly covering any emitted Hawking photons. With these issues in mind, we recently proposed an alternative approach to generating controllable dielectric perturbations, namely ultrashort laser pulse filamentation [10].

3. Ultrashort laser pulse filamentation

Ultrashort laser pulse filamentation may be defined as the creation of an intense laser pulse in a transparent Kerr medium (i.e. with a third-order optical nonlinearity) characterized by a high-intensity spike that propagates apparently without diffraction over distances much longer than the Rayleigh length associated with the spike transverse dimensions. Filaments may occur spontaneously, when a powerful Gaussian-shaped beam is loosely focused into the Kerr medium [20, 21], or alternatively they may be induced by preshaping the laser pulse into a Bessel beam [22, 23].

3.1. Spontaneous filaments

The mechanism underlying the formation of a spontaneous filament is the interaction between the intense laser pulse and the medium Kerr nonlinearity, which induces a reshaping of the pulse along both the transverse (y, z) and longitudinal (x) coordinates. In the transverse plane, the input pulse will start to shrink under the so-called self-focusing effect, and in the longitudinal coordinate, self-phase modulation and dispersion will create new frequencies and distort the pulse. These effects occur concomitantly and the input pulse is focused to a so-called nonlinear focus point at which the highest intensity is reached. This intensity is typically ‘clamped’ to

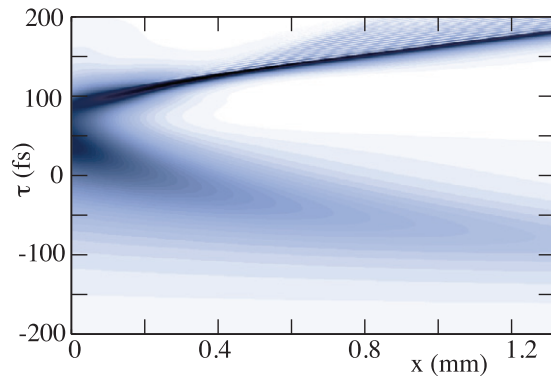


Figure 1. Numerically calculated (x, t) profile of a spontaneous filament in fused silica in the region immediately after the nonlinear focus. The pulse splits into two daughter pulses. The trailing pulse is compressed with a nearly single cycle shock front and maintains a high nearly constant intensity over a distance ~ 1 mm.

a maximum value that depends mainly on the material properties (e.g. dispersion, nonlinear absorption and ionization) and will vary only slightly with the laser pulse input energy. After the nonlinear focus, a filament will emerge; that is, in the transverse plane, a tightly focused intensity spike is observed that propagates apparently without diffraction over long distances. This intensity is surrounded by a much weaker photon reservoir, which co-propagates with the intensity spike and continues to refuel it. The intensity of the central spike will typically start to decay, concomitantly with the formation of two split daughter pulses, one travelling faster and the other slower with respect to the input laser pulse [20].

It is important to note that the interplay between the various linear (dispersion and diffraction) and nonlinear (self-phase modulation, self-steepening, multiphoton absorption and ionization and plasma creation) effects leads to very complicated dynamics that may be collectively described only qualitatively by analytical models. A quantitative prediction of the full spontaneous filament evolution relies on numerical simulations. These are usually based on the numerical solution of the extended nonlinear Schrödinger equation [20]. This equation is also used in this work to model filament propagation and gives, as an example, the results shown in figures 1 and 2. Figure 1 shows the evolution of the temporal profile at $y = z = 0$ (i.e. at the pulse centre in the transverse dimensions y and z) along the comoving longitudinal coordinate $\tau = t - x/v$, where v is the input Gaussian pulse velocity v_G . The evolution is shown just after the nonlinear focus as the pulse clearly splits into two daughter pulses with the trailing (leading) pulse travelling slower (faster) than the input pulse. Moreover, the self-compression of the longitudinal dimension of each of these pulses is also evident. Figure 2(a) shows a line-out of this figure for three different propagation distances so as to highlight the pulse-splitting features. Figure 2(b) shows in more detail the velocity v of the trailing daughter pulse over a distance that roughly spans the region analysed in our experiments (described below). The coloured points (blue, green and red) indicate the propagation distances at which the longitudinal profiles are sampled and shown in figure 2(a) (with the same colours). As can be seen, the pulse velocity at the nonlinear focus is significantly lower than $v_G \sim 2.05 \times 10^8 \text{ m s}^{-1}$ and accelerates during propagation, asymptotically reaching v_G . This behaviour is qualitatively reproduced in all spontaneous filaments and the details, e.g. the precise values of the pulse

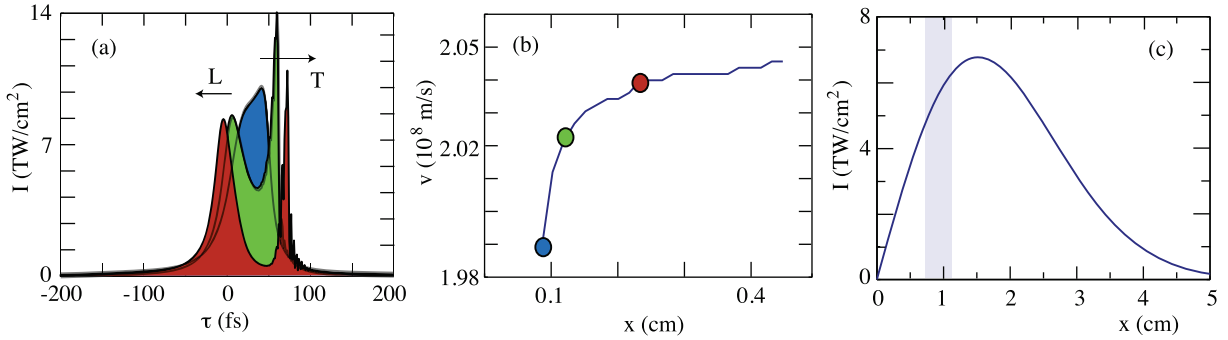


Figure 2. (a) Numerically calculated temporal profile of the filament pulse: close to the nonlinear focus the pulse splits into a faster, leading (L) and a slower, trailing (T) pulse. (b) The variation of the trailing peak (T) velocity with propagation distance. (c) Evolution of the peak intensity in a Bessel filament calculated using equation (1). The shaded region indicates the region imaged and analysed in the experiments.

velocities, depend on the specific experimental settings and mainly on the input wavelength, the input pulse duration and the Kerr medium.

The input parameters used for the simulation in figures 2(a) and (b) were chosen to reproduce those of the experiments, i.e. 1 ps pulse duration, 1055 nm laser wavelength, 0.3 mJ input energy and $w_0 = 0.5 \text{ mm}$ input width at $1/e^2$. The pulse was loosely focused with a 20 cm focal length lens into a 2 cm-long sample of fused silica (FS). These input conditions lead to the pulse shapes shown in figure 2(a). The transverse profile (not shown) is characterized by a localized central peak that has a diameter of $\sim 5 \mu\text{m}$.

3.2. Bessel filaments

A tightly focused, high-intensity peak that propagates with negligible diffraction in nonlinear Kerr media may also be formed by preshaping the Gaussian beam into a so-called Bessel beam. The Bessel beam exhibits significant differences with respect to a Gaussian beam. These differences are best visualized by considering the far-field pattern or the Fourier spectrum. A Gaussian beam may be viewed as the sum of infinite plane waves with wave vectors in the transverse plane (k_y, k_z) whose amplitudes are weighted with a Gaussian function centred at $k_z = k_y = 0$. The Bessel beam spectrum is a ring in the (k_y, k_z) plane, i.e. the plane waves propagate at an angle with respect to the propagation direction and are thus distributed along a conical surface characterized by a well-defined cone angle $\theta = \tan^{-1}(k_z/K)$, where $K = \omega n/c$ is the modulus of the plane-wave wave vector with frequency ω , and in a medium with refractive index n . In the near field, the azimuthal symmetric interference pattern of the overlapping plane waves is described by the zero-order Bessel function. The central peak is therefore simply the result of an interference pattern which is continuously reconstructed along the propagation direction and propagates without diffraction. The cone angle θ may be adjusted so as to achieve a tighter central peak with a higher intensity. Even more importantly, due to the off-axis propagation of the plane-wave components, the effective group velocity of the Bessel peak also depends on the cone angle as $v = v_G/\cos \theta$.

A Bessel beam may be obtained experimentally by sending a collimated Gaussian beam through an axicon, i.e. a conical prism. The angle θ of the output Bessel beam is related to

the axicon base angle γ by Snell's law of refraction that gives the relation $n_{\text{air}} \sin(\theta + \gamma) = n_{\text{axicon}} \sin \gamma$, where n_{air} and n_{axicon} are the refractive indices of the surrounding medium (usually air) and of the axicon material (typically FS), respectively. Using the fact that the input pulse is Gaussian, it is also possible to determine the evolution of the peak intensity along the propagation direction x [24]:

$$I(x) = I_0 2\pi K x \tan^2 \theta \exp\left(-\frac{x^2 \tan^2 \theta}{w_0^2}\right), \quad (1)$$

where I_0 and $\sqrt{2}w_0$ are the input Gaussian peak intensity and radius at $1/e^2$. The full three-dimensional (3D) profile of the Bessel pulse is described by $I(x, r, t) = I(x)I(r)I(t)$, where $I(x)$ is given by equation (1) and $I(r) = J_0(Kr \sin \theta)$, and the temporal profile is given by the input Gaussian profile $I(t) = \exp(-((x - vt)/\sigma_t)^2)$. A plot of equation (1) is shown in figure 2(c), which gives the peak intensity of the Bessel filament, for the input Gaussian pulse used in the experiments (see below), i.e. with 1 ps duration, $w_0 = 5$ mm and $I_0 = 1$ GW cm $^{-2}$. The shaded area highlights the region imaged and analysed in the experiments.

Therefore, we see that, in contrast to the spontaneous filament, the Bessel filament allows direct control of both the pulse velocity and the pulse peak intensity. However, if the Bessel filament is generated with an axicon, v may only be made larger than v_G while the spontaneous filament delivers two pulses, one faster than and the other slower than v_G . We note that in our experiments, we used a $\gamma = 20^\circ$ base angle FS axicon that produced a $\theta \simeq 7^\circ$ Bessel pulse in the FS sample. The diameter at $1/e^2$ is $5.9 \mu\text{m}$ and is very similar to the $\sim 5 \mu\text{m}$ diameter of the spontaneous filament and also has a similar peak intensity (compare figures 2(a) and (c)). Thus, experiments with the spontaneous and Bessel filaments were conducted under very similar input conditions from the point of view of pulse diameter and intensity.

Finally, an important feature of Bessel pulses is the possibility of strongly suppressing or even completely eliminating the modulation instability and the formation of supercontinuum [22]. At very high intensities, not used in our experiments, the Bessel pulse may break up under the influence of instabilities and may exhibit similar dynamics to the spontaneous filament. However, at the intensities used here, similar to those reached by the spontaneous filament, no strong nonlinear effects related to nonlinear phase accumulation occur in virtue of the fact that the energy density flux is directed along a cone with a relatively large angle. This therefore drastically reduces nonlinear effects, which require significant on-axis (i.e. at zero or low angle) propagation distances to accumulate. Indeed we observe no continuum generation, in stark contrast to the spontaneous filament case. The ability to suppress any background or spurious radiation is extremely important in order to measure background-free signals. This suppression is obtained by placing the nonlinear Kerr medium as close as possible to the axicon so as to enter the medium with as low an intensity as possible. The Bessel peak intensity then grows slowly inside the sample and modulation instabilities are not amplified so that the pulse propagates without significant spectral or temporal distortion [23]. This specific propagation regime was adopted in our experiments.

4. Propagation equations and the creation of horizons using laser pulses

We will be able to understand in slightly more detail how a horizon is formed by a laser pulse by deriving the basic propagation equation that describes how a weak probe field propagates in the presence of an intense pump laser pulse. In the following, we sketch a relatively simple

and intuitive method for deriving a *linear* propagation equation that describes the interaction of an electromagnetic field with the dielectric perturbation that is, in turn, generated by the laser pump pulse. We start from the general equation for the electric field in a dielectric medium:

$$\nabla \times (\nabla \times \mathbf{E}) + \mu_0 \partial_t^2 \mathbf{P} + \frac{1}{c^2} \partial_t^2 \mathbf{E} = 0. \quad (2)$$

Using $\nabla \times (\nabla \times \mathbf{E}) \simeq -\nabla^2 \mathbf{E}$, we obtain

$$\partial_x^2 \mathbf{E} + \partial_\perp^2 \mathbf{E} - \mu_0 \partial_t^2 \mathbf{P} - \frac{1}{c^2} \partial_t^2 \mathbf{E} = 0. \quad (3)$$

We then write the material polarization as⁹.

$$\mathbf{P} = \varepsilon_0 (\chi^{(1)} \mathbf{E} + \chi^{(3)} (\mathbf{E} \cdot \mathbf{E}) \mathbf{E} + \dots). \quad (4)$$

Regarding the nonlinear polarization term, we make the assumption that \mathbf{E} is the sum of two fields: an intense pump field oscillating at frequency ω_p , $\mathbf{E}_p = \mathcal{E}_p \exp(i\omega_p t) + \text{c.c.}$, and a probe field oscillating at frequency ω_s , $\mathbf{E}_s = \mathcal{E}_s \exp(i\omega_s t) + \text{c.c.}$. Consequently, $(\mathbf{E} \cdot \mathbf{E}) \mathbf{E} = (\mathbf{E}_p \cdot \mathbf{E}_p) \mathbf{E}_p + (\mathbf{E}_s \cdot \mathbf{E}_s) \mathbf{E}_s + (\mathbf{E}_s \cdot \mathbf{E}_s) \mathbf{E}_p + 2(\mathbf{E}_p \cdot \mathbf{E}_s) \mathbf{E}_s + (\mathbf{E}_p \cdot \mathbf{E}_p) \mathbf{E}_s + 2(\mathbf{E}_p \cdot \mathbf{E}_s) \mathbf{E}_p$. The first term will describe the self-action of the pump field on itself and the second, third and fourth terms may be neglected due to the assumption that \mathbf{E}_s is very weak. The only terms of interest for the present discussion are therefore the last two terms that will describe the action of the pump field, mediated by the material polarization, on the weak probe field. We write therefore

$$\mathbf{P} = \varepsilon_0 (\chi^{(1)} + \chi^{(3)} (\mathbf{E}_p \cdot \mathbf{E}_p)) \mathbf{E}_s + 2\varepsilon_0 \chi^{(3)} (\mathbf{E}_p \cdot \mathbf{E}_s) \mathbf{E}_p. \quad (5)$$

We can read this formula by stating that there is a non-homogeneous and non-stationary susceptibility

$$\chi = \chi^{(1)} \mathbf{I} + \chi^{(3)} ((\mathbf{E}_p \cdot \mathbf{E}_p) \mathbf{I} + 2\mathbf{E}_p \otimes \mathbf{E}_p) \quad (6)$$

whose amplitude depends on the pump field \mathbf{E}_p . By substituting the given forms of the electric fields, we find that, in components,

$$\begin{aligned} \chi_{ij} = & \chi^{(1)} \delta_{ij} + \chi^{(3)} (\mathcal{E}_p^2 e^{i2\omega_p t} + \mathcal{E}_p^{2*} e^{-i2\omega_p t} + 2|\mathcal{E}_p|^2) \delta_{ij} \\ & + 2\chi^{(3)} (\mathcal{E}_{pi} \mathcal{E}_{pj} e^{i2\omega_p t} + \mathcal{E}_{pi}^* \mathcal{E}_{pj}^* e^{-i2\omega_p t} + \mathcal{E}_{pi} \mathcal{E}_{pj}^* + \mathcal{E}_{pi}^* \mathcal{E}_{pj}). \end{aligned} \quad (7)$$

Taking $\mathbf{P} = \varepsilon_0 \chi \mathbf{E}_s$ and substituting the given form for \mathbf{E}_s , one can see that there are $\chi^{(3)}$ -terms that oscillate at frequency $2\omega_p$ and will scatter the probe wave to frequencies $2\omega_p \pm \omega$. These terms describe parametric four-wave mixing (FWM) or third harmonic generation and optical rectification in the degenerate case $\omega_p = \omega$. We shall neglect these terms, as the effects of FWM are well known [25] and do not enter the specific scattering mechanism we are interested in, i.e. Hawking emission. The remaining terms in equation (7) are dc terms; that is, they do not oscillate but rather describe an instantaneous variation in the susceptibility, and hence also in

⁹ In components, one has

$$P_i = \sum_j \chi_{ij}^{(1)} E^j + \sum_{j,k} \chi_{ijk}^{(2)} E^j E^k + \sum_{j,k,l} \chi_{ijkl}^{(3)} E^j E^k E^l + \dots$$

Assuming that the dielectric is isotropic, one has $\chi_{ij}^{(1)} = \chi^{(1)} \delta_{ij}$, $\chi_{ijk}^{(2)} = 0$ and $\chi_{ijkl}^{(3)} = \chi_{xxyy}^{(3)} \delta_{ij} \delta_{kl} + \chi_{xyxy}^{(3)} \delta_{ik} \delta_{jl} + \chi_{xyyx}^{(3)} \delta_{il} \delta_{jk}$, so that $P_i = \chi^{(1)} E_i + \chi^{(3)} (\mathbf{E} \cdot \mathbf{E}) E_i$, where $\chi^{(3)} := \chi_{xxxx}^{(3)} = \chi_{xxyy}^{(3)} + \chi_{xyxy}^{(3)} + \chi_{xyyx}^{(3)}$.

the refractive index, that travels with the pump pulse and may scatter the probe pulse. It is these terms that are responsible for generating the dielectric perturbation that travels at the pump-pulse group velocity and that, under appropriate conditions described below, forms a horizon and can excite Hawking radiation.

Returning now to the wave equation (3), assuming that the amplitude $|\mathbf{E}_p|^2$ varies slowly with respect to the field \mathbf{E}_s , we find that

$$\left(\partial_x^2 + \partial_\perp^2 - \frac{1}{c^2} (1 + \chi^{(1)} + \chi^{(3)} |\mathbf{E}_p|^2) \partial_t^2 \right) \mathbf{E}_s = \frac{2}{c^2} \chi^{(3)} \partial_t^2 ((\mathbf{E}_p \cdot \mathbf{E}_s) \mathbf{E}_p). \quad (8)$$

We finally take the eikonal approximation for the plane wave, which, together with the observation that in our experiments (see below) we only detect photons \mathbf{E}_s that are orthogonally polarized with respect to the input pump pulse, \mathbf{E}_p , leads to

$$\left(\partial_x^2 + \partial_\perp^2 - \frac{1}{c^2} (1 + \chi) \partial_t^2 \right) \mathbf{E}_s = 0. \quad (9)$$

We emphasize that this may be viewed as a *linear* wave equation; that is, once the effect of the nonlinear polarization term is encompassed in the generalized non-homogeneous and non-stationary susceptibility χ , there are no further material nonlinearities, and the problem of how a weak probe pulse interacts with the dielectric perturbation generated by the intense pump pulse should be viewed as a linear scattering process mediated by χ .

5. The metric and horizon condition

In [26, 27], we have studied in detail both the derivation and properties of the analogue metric associated with the eikonal approximation of the field equations. Herein, we limit ourselves to recalling that the metric in the laboratory frame can be written as follows [26]:

$$g_{\mu\nu} = \text{diag} \left(\frac{c^2}{n^2}, -1, -1, -1 \right), \quad (10)$$

where $n = \sqrt{1 + \chi^{(1)} + \chi^{(3)} |\mathbf{E}_p|^2}$ is the refractive index.

We note that this metric is defined up to a conformal factor Ω . This factor does not change the null geodesics, or light paths, that may derived from the metric but it may, *a priori*, influence the spectral emission features. It has been demonstrated, however, that for the above metric the conformal factor cancels out in the derivation of the surface temperature and in the calculations of the emitted spectra so that it may therefore be safely neglected [27, 28].

The two-dimensional (2D) version of this metric (i.e. neglecting any dependence on the coordinates transverse to the propagation direction) is

$$ds^2 = \frac{c^2}{n^2(x - vt)} dt^2 - dx^2. \quad (11)$$

We then pass from the laboratory frame to the pulse frame (perturbation frame) by means of a boost: $t' = \gamma(t - \frac{v}{c^2}x)$, $x' = \gamma(x - vt)$, so that

$$\begin{aligned} ds^2 = & c^2 \gamma^2 \frac{1}{n^2} \left(1 + \frac{nv}{c} \right) \left(1 - \frac{nv}{c} \right) dt'^2 \\ & + 2\gamma^2 \frac{v}{n^2} (1 - n^2) dt' dx' - \gamma^2 \left(1 + \frac{v}{nc} \right) \left(1 - \frac{v}{nc} \right) dx'^2. \end{aligned} \quad (12)$$

Here, $n(x')$ represents a perturbation induced by the laser pulse on the top of a uniform background refractive index, n_0 , i.e. $n(x') = n_0 + \delta n f(x')$, where $f(x')$ is a function limited between 0 and 1 that describes the shape of the laser pulse and $\delta n = n_2 I$, where n_2 is the nonlinear Kerr index and I is the laser pulse peak intensity. In general, $\delta n \ll n_0$ in experimental situations.

There is an ergosurface $g_{00} = 0$, i.e. for $1 - nv/c = 0$, which moreover turns out to be lightlike and, in the 2D case, to correspond to a horizon [26, 27], under the conditions

$$\frac{1}{n_0 + \delta n} < \frac{v}{c} < \frac{1}{n_0}. \quad (13)$$

This condition predicts the dielectric perturbation velocities for which a horizon is formed. We note that although it is derived in the absence of dispersion, the same condition appears to apply also in the case of material dispersion with the additional feature that n_0 becomes a function of frequency [27]. This fact, although lacking an *a priori* justification, has been directly verified by numerical simulations based on the Maxwell equations (as shown below). Equation (13) plays an important role in the present work as it is used to predict the wavelength regions in which we expect to observe Hawking radiation. Moreover, the dependence of the wavelength window on the perturbation velocity is a clear indication that sets aside this effect from any other known to date, and in the following, it is used as proof of the horizon-related origin of the measured photons.

6. A comment on the horizon condition

A crucial point that renders experiments viable is the frequency dependence of n , i.e. material dispersion. In the absence of dispersion a horizon is created only if v is tuned with extreme care such that equation (13) is satisfied. Bearing in mind the small values of $\delta n \sim 10^{-3}$ – 10^{-4} (e.g. in FS, $n_2 \sim 3 \times 10^{-16} \text{ cm}^2 \text{ W}^{-1}$ [25, 29] and $I \sim 10^{13} \text{ W cm}^{-2}$), this would be no minor feat. Conversely, in the presence of dispersion, $n = n(\omega)$ and equation (13) defines a horizon and a spectral emission region for *any* value of v . Figure 3 shows the predicted spectral regions for the following three cases: (a) the trailing daughter pulse within a spontaneous filament with v taken from figure 2(a); (b) a Gaussian pulse propagating with $v = v_G$; (c) a Bessel filament propagating with $v = v_G/\cos\theta$ and $\theta = 7^\circ$. Two curves are shown in each graph: the refractive index n and $n + \delta n$ with $\delta n = 0.001$. We emphasize that the Hawking photons will be emitted only in a bounded spectral window. This is somewhat different from the dispersionless case in which, once v is properly tuned so as to achieve the horizon condition, all frequencies are excited. In the presence of dispersion as in our analogue model, only a limited spectral region is excited and the blackbody spectral shape, typically associated with Hawking radiation, will not be discernible.

Regarding the width of the spectral emission window, we note that this is determined by the values of both v and δn . If the perturbation moves with the same velocity as that of a Gaussian pulse centred at 1055 nm, $v = v_G(1055 \text{ nm}) = \text{constant}$ and Hawking emission will be centred around 500 nm with a ~ 20 nm bandwidth. The Bessel filament will have a larger velocity and emission is expected to be around 850 nm with larger bandwidth, ~ 60 nm, due to the lower dispersion at these wavelengths. Conversely, in the case of the spontaneous filament, the variation of v along the propagation direction dominates the emission characteristics and emission is predicted around 350 nm with ~ 200 nm bandwidth. The δn induces only a minor 5–10 nm broadening at these wavelengths.

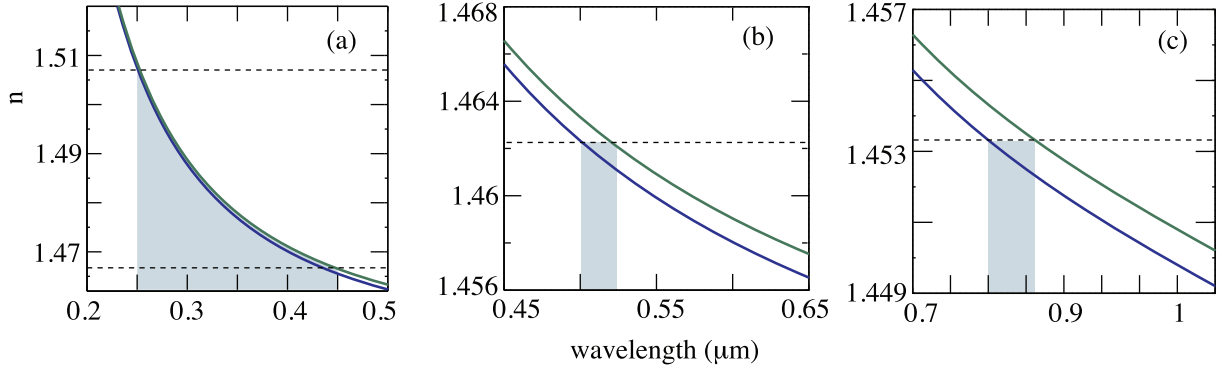


Figure 3. Prediction of the Hawking emission spectral range based on the dielectric perturbation velocity v and the medium (FS) refractive index. Blue curves represent the background refractive index n_0 and the green curves represent $n_0 + \delta n$. (a) Spontaneous filament: the filament perturbation velocity covers a broad range of values, evaluated from numerical simulations. (b) Gaussian pulse: $v = v_G$ is determined by the material dispersion. (c) Bessel filament: $v = v_G / \cos \theta$. In all cases $\delta n = 0.001$.

A further issue that then needs to be discussed is the role played by the variation of v_g , i.e. of the dielectric perturbation acceleration. Figure 2(b) shows the evolution of the trailing filament pulse (indicated by T in figure 2(a)). We should therefore consider the possibility that the acceleration itself could somehow modify the nature of the emitted photons. For example it is predicted that an accelerated observer will perceive the background at a higher temperature with respect to an observer in an inertial reference frame. We may qualitatively rule out such effects by noting first of all that the actual variation of velocity is only of the order of a few per cent of the initial pulse velocity and may thus be locally considered as a small ‘perturbation’ of the ideal, constant-velocity case. Moreover, in analogy with a similar reasoning followed by Ginzburg and Frolov [30], we note that Hawking photons are expected to be excited from the vacuum in a time, τ , that is the inverse of their frequency (i.e. the photons become real once they are separated by a distance that is at least equal to their wavelength, λ). In the UV region expected for our experiments in FS, $\tau \sim \lambda / cn_0 \sim 1$ fs. This time is 3 orders of magnitude smaller than the ~ 1 ps interval during which the laser pulse accelerates, thus implying that any acceleration-related effects are expected to be negligible on the time scale of Hawking photon production effects.

Finally, we emphasize that it has been shown that electromagnetic waves will experience a logarithmic phase divergence at these horizons [27]. We may briefly summarize the origin of this divergence as follows. The horizon condition arises in the equations for the electromagnetic field from the condition $F = 1 - n(u_+)v/c = 0$: at this point the equations develop a Fuchsian singularity in $u = u_+$. This arises as a result of F multiplying the u derivatives, and on inspection one sees that at least one of the critical exponents has a non-vanishing imaginary part. Therefore, there is a solution ϕ having the form $\phi(u) \sim (u - u_+)^{\alpha+i\beta}$ near the horizon, with $\beta \neq 0$, which leads to a logarithmically diverging phase. Generally speaking, this divergence is exactly of the same nature as the divergence highlighted by Hawking in his original work and is crucial in the mode conversion process that leads to amplification of vacuum fluctuations [14, 31, 32]. This phase divergence therefore lies at the heart of Hawking emission and is one of its characterizing features. In the absence of dispersion the phase divergence will be infinite and eventually leads

to trans-Planckian wavelengths (the so-called trans-Planckian problem). However, dispersion curbs this divergence and limits it well before unknown physical regimes are reached. Indeed, as the electromagnetic wave is blue-shifted by the phase increase at the horizon, it also slows down due to the increasing dispersive refractive index. Eventually the wave will be slowed down so much that it will be left behind by the dielectric perturbation and will therefore detach from the horizon.

7. Stimulated Hawking emission (SHE) and thermality: numerical simulations

Hawking emission is ‘seeded’ by the vacuum state and this therefore implies that information on the features of the emission process may be gained by directly seeding the conversion process with a large-amplitude, classical pulse. We call this stimulated Hawking emission (SHE). Indeed, SHE plays a fundamental role in those analogous systems that cannot resort to the study of quantum vacuum but have nevertheless allowed one to demonstrate remarkable results related to Hawking emission. The most important example in this context is mode conversion in water waves. SHE is predicted to lead to mode conversion from the input (IN) wave to two output waves that have positive (P-mode) and negative (N-mode) frequencies in the comoving reference frame. The first observation of the generation of negative frequency modes was given by Rousseaux *et al* [33], and more recently, the process was shown by Weinfurter *et al* [34] to also exhibit a thermal-like behaviour. This highlights the importance of these studies. Indeed, taking the ratio of the squared amplitudes of the P and N modes, $R = |N|^2/|P|^2$, together with the condition that $|P|^2 - |N|^2 = 1$, allows one to directly evaluate the nature of Hawking emission also in the spontaneous regime. The above relations allow one to write the number of particles emitted from the horizon as $\langle \mathcal{N} \rangle = R/(1 - R)$. If $R = \exp(-C\nu)$ is a negative exponential function of frequency ν , then the emitted spectrum $\langle \mathcal{N} \rangle = 1/(\exp(C\nu) - 1)$ is thermal. Blackbody emission is a standard result of the Hawking emission process and is often regarded as one of its fundamental traits. However, it is important to point out that this result was originally derived without dispersion. We may readily understand at a qualitative level what the impact of dispersion will be in our case. We recall that the emission temperature in the dispersionless case is determined by the gradient of the dielectric perturbation at the horizon, i.e. at the point for which $v = c/n$. In the presence of dispersion the horizon condition becomes a function of frequency $v = c/n(\omega)$, i.e. the position of the horizon within the dielectric perturbation depends on frequency and therefore so does the perturbation gradient. This in turn implies that within the emission frequency window predicted by equation (13), the gradient and temperature will vary between some minimum and maximum values. In such a situation, it clearly loses meaning to refer to a blackbody spectrum of any kind. This reasoning is in keeping with recent works in analogue dispersive systems in which the emission from a dispersive white hole may not even bear the expected relationship with the surface gravity (i.e. velocity or perturbation gradient) [35] and has been shown to have a flat spectrum [36] in stark contrast with the well-known blackbody emission. Notwithstanding, in agreement with these works, we continue to refer to the process as Hawking emission in view of the fact that the fundamental ingredients that are unique to this process, i.e. the amplification of vacuum fluctuations as a result of a logarithmic phase divergence in the dispersionless case, or phase accumulation in the presence of dispersion at the horizon, are preserved [26, 27].

Therefore, following the same rationale described above, we performed numerical simulations of SHE with the aim of explicitly evaluating R and thus the characteristics of the

spectral emission in the presence of dispersion in our system. The numerical code performs 2D (time and one spatial coordinate) simulations based on equation (3), neglecting the transverse coordinate derivatives. The equation is solved using the Yee scheme [37], which also includes a quadratic variation of the refractive index versus frequency that was chosen to match the dispersion of FS glass in the visible to near-infrared spectral range. We note that equation (3) is somewhat more general than the equation (8) used also in demonstrating the Hawking emission for the dielectric perturbation analogue [27]. Indeed, this last equation is valid in the limit in which the perturbation varies slowly with respect to the input seed wavelength, while no approximations are made when solving equation (3). Nevertheless, as we show below, Hawking-like mode conversion with a clear thermal signature is observed in all situations, i.e. when the dielectric perturbation has both small and large gradients. This shows that SHE is far more general than what may be expected from a simplified analytical treatment ([27]).

Here, we limit ourselves to the presentation of some very basic results, as a full description of the model, physics and implications of the SHE process is beyond the scope of the present work and shall be the subject of a future publication. The results of the simulations are shown in figure 4.

Figure 4(a) shows a zoom-in of the trailing edge of the dielectric perturbation where the horizon is formed, while figure 4(b) shows the dispersion relation, in the comoving reference frame, experienced by an optical pulse approaching the perturbation along the x -coordinate. The colour coding is a guide to the eyes and reflects the amplitude of the perturbation in that position.

The dispersion relation in figure 4(b) is determined from the dispersion relation in the laboratory reference frame $k = (\omega/c) \cdot [n(\omega) + \delta n_0]$, as $\omega' = \gamma(\omega - vk)$ and $k' = \gamma[k - (v/c^2)\omega]$, where primed quantities indicate that they refer to the comoving reference frame and δn_0 indicates the amplitude of the dielectric perturbation at the relevant horizon. We note that above a certain critical value of δn_0 , mode conversion can no longer occur as the dispersion curve decreases monotonically (dashed curves). This shows that, contrary to what one may intuitively expect, increasing the maximum amplitude of the perturbation will not necessarily lead to a wider emission window once this critical value is reached.

In figure 4(c), we have selected a single dispersion curve, $\delta n_0 = 2.4 \times 10^{-3}$, to illustrate the relationship between the input and the mode-converted frequencies. The input frequency ω'_{in} selects two points on the dispersion curve: the IN mode and the output positive P mode. In the Hawking conversion process a second, negative N, output mode is also created at $-\omega'_{\text{in}}$. The point indicated with PH indicates the phase horizon for which, in the comoving frame, the field has zero frequency $\omega'_{\text{in}} = 0$ but non-zero wavelength, $k' \neq 0$. The two Hawking modes are always generated to the left and to the right of the horizon point. Figures 4(e)–(g) show the results of a numerical simulation with an input wavelength of $4 \mu\text{m}$ and perturbation velocity $v = 0.996c$. The red shaded area shows the dielectric perturbation longitudinal profile (scaled so as to render it clearly visible). The pulse is shown at three different times: at the input ($t = 0$ ps); at an intermediate stage ($t = 15$ ps), clearly showing how the input pulse is blocked at the dielectric perturbation and frequency converted; and at the output ($t = 45$ ps), i.e. when the pulse has been completely converted shifted to blue-shifted wavelengths and thus, due to dispersion, separates from the dielectric perturbation and starts to lag behind. We emphasize that the input pulse is blocked in virtue of the fact that it encounters a group-velocity horizon, i.e. a point at which the pulse group velocity, v_g , equals the perturbation velocity. Indeed, at a slightly higher $\delta n_0 = 3.7 \times 10^{-3}$ the dispersion curve will bend further down (dark red

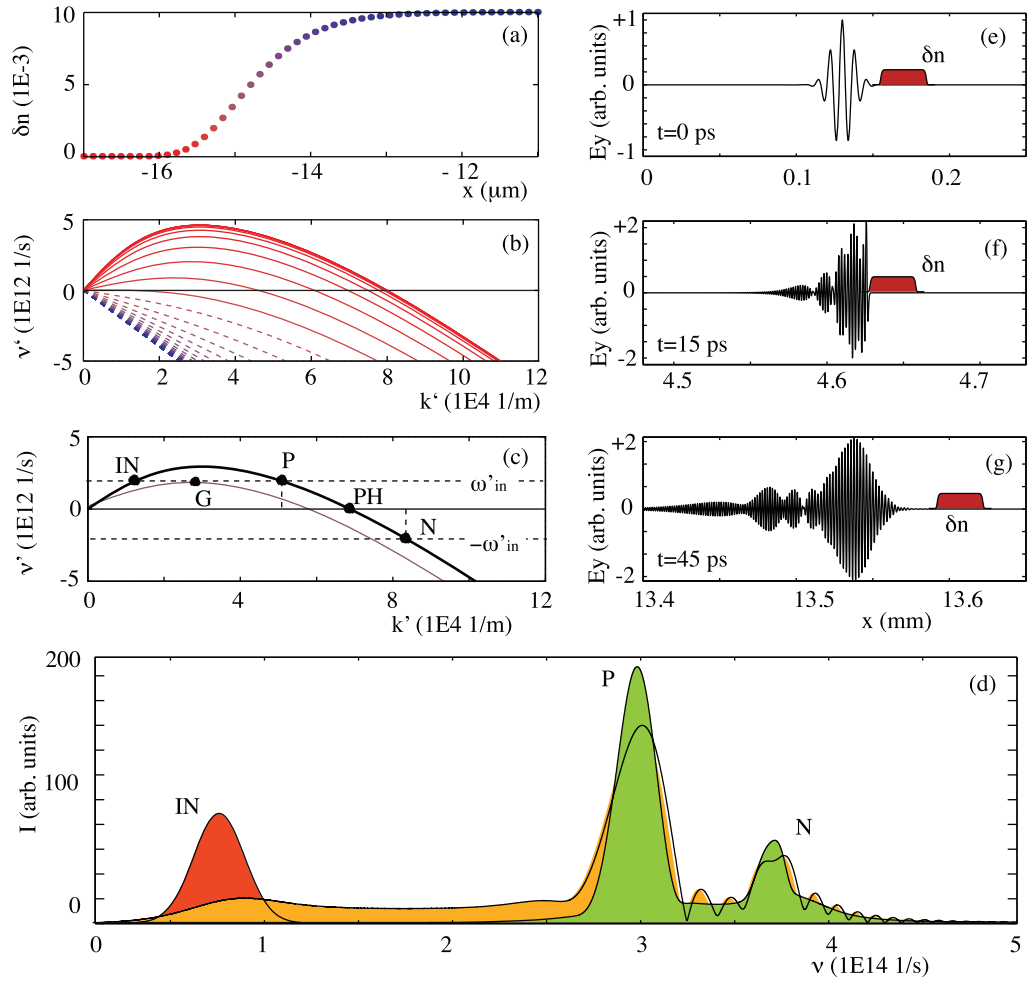


Figure 4. Stimulated Hawking mode conversion. (a) Trailing edge of the perturbation where the horizon is formed; (b) dispersion relation in the comoving reference frame, for increasing values of the perturbation amplitude, following the same colour code as that in (a). Above a certain critical value of δn , mode conversion can no longer occur as the dispersion curve decreases monotonically (dashed curves). (c) The input frequency ω'_{in} selects two points on the dispersion curve: the IN mode and the output positive P mode. In the Hawking conversion process, a second, negative N, output mode is also created at $-\omega'_{\text{in}}$. PH indicates the ‘phase horizon’ for which, in the comoving frame, the field has zero frequency $\omega'_{\text{in}} = 0$ but non-zero wavelength ($k' \neq 0$). (e–g) the results of a numerical simulation with an input wavelength of $4 \mu\text{m}$. The red shaded area shows the dielectric perturbation (scaled so as to render it clearly visible). The pulse is shown at three different times: at the input ($t = 0$ ps), at an intermediate stage ($t = 15$ ps) and at the output ($t = 45$ ps). (d) The spectrum for the three pulses in (e), (f) and (g). The input spectrum IN is converted into two P and N Hawking modes, centred at wavelengths of 1 and $0.8 \mu\text{m}$, respectively.

thin curve in the figure) so that the IN mode falls at the extremum of the dispersion curve, i.e. $v_g = 0$. The input pulse may therefore propagate no further (in the comoving reference frame). More details of the nature of the horizons encountered in these analogue gravity systems

are given below, although a precise formulation of the relationship between these and their relative role in Hawking mode conversion requires a separate study, which is beyond the scope of the present work.

Figure 4(d) shows the spectrum for the three pulses in (e)–(g). The input spectrum IN is converted into two P and N Hawking modes, centred at wavelengths of 1 and $0.8\ \mu\text{m}$, respectively. We note that we have explicitly verified that the P and N modes do indeed exhibit opposite constant-phase slopes in the comoving reference frame, thus proving that they do indeed correspond to positive and negative frequency modes according to the recipe described in [33]. The beating between these two modes is the origin of the slow-amplitude oscillations in the output field in (g).

We recall that we set out with these simulations in order to evaluate quantitatively the ratio $R = |N|^2/|P|^2$ between the total energies located in the negative and positive mode peaks (obtained by integrating over each P and N spectral peak separately). The results are shown in figure 5. The simulations were performed with two different approaches: (i) with fixed perturbation velocity and varying input frequency; (ii) with varying dielectric perturbation velocity and fixed input frequency.

(i) The first set of simulations was performed with a fixed perturbation velocity and a varying input frequency in the laboratory reference frame. Figure 5(a) shows the relevant dispersion relation: we found that each input frequency experiences a very similar horizon and therefore also sees the same dispersion relation at the horizon. The reason for this is related to the fact that although the horizon position, u , will and must depend on the input frequency ω_0 , this dependence is actually very weak. Indeed, using the parameters for the numerics, it is possible to verify that

$$\left. \frac{1}{u(\omega_0)} \frac{du}{d\omega} \right|_{\omega_0} \delta\omega \ll 1. \quad (14)$$

This implies that the horizon shift with frequency is sufficiently small so that it does not perturb the thermality of the outcoming modes. Indeed, the blue circles in figure 5(b) show that R follows an exponential law with the best fit (blue solid line) given by $R = 1.01 \exp(-1.87 \times 10^{-12} \nu')$: for $\nu' = 0$, we have $R \sim 1$ to a very good approximation, as should be expected and, most importantly, the decay constant $C = \hbar/k_B T_H = 1.87 \times 10^{-12}\ \text{s}$ is directly related to the Hawking temperature T_H . We thus obtain $T_H = 25.6\ \text{K}$ (or $T_H = 1479\ \text{K}$ in the laboratory reference frame), which we may compare with the predicted temperature, equation (16), given below and with the gradient of the dielectric perturbation calculated at the horizon, $T_H = 24\ \text{K}$.

The other data points and curves in figure 5(b) correspond to two additional sets of numerical simulations performed with different gradients, corresponding to the laboratory-frame temperatures of $T = 707\ \text{K}$ (in red) and $T = 3486\ \text{K}$ (in green). In all cases the best fit is exponential, thus showing that thermal Hawking-like emission is observed over a wide range of parameters that actually extend beyond the approximations performed in order to carry out the analytical treatment in [27].

These results therefore clearly show that under conditions in which the horizon depends only weakly on the input frequency, a thermal output spectrum will be observed in agreement with Hawking's predictions extended to our analogue setting. A surprising observation is that, notwithstanding the background dispersion, the extrapolated temperature is actually in excellent agreement with the predicted value (albeit slightly higher), based on a theory that does not

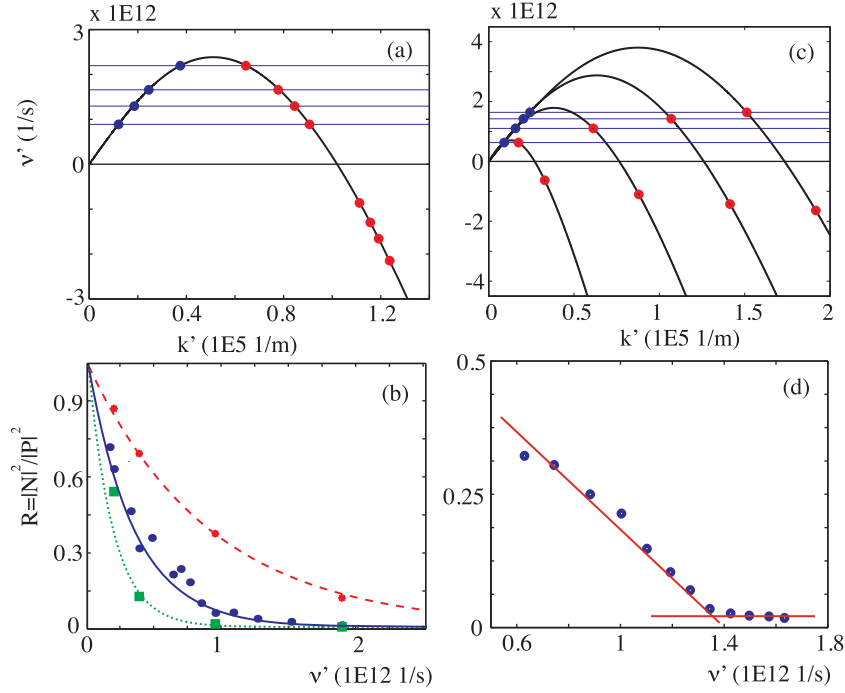


Figure 5. Numerical evaluation of the ratio R between the positive and negative modes for two different sets of experiments. Frequency-independent horizon: (a) All input frequencies experience the same δn_0 and refractive index gradient. (b) Blue circles: $R = |N|^2/|P|^2$ versus input frequency for the same perturbation as in (a), shows a clear exponential dependence with best fit $R = 1.01 \exp(-1.1 \times 10^{-12} \nu')$ (blue solid curve), corresponding to a blackbody emission with temperature $T = 25.6$ K ($T = 1479$ K in the laboratory frame), to be compared with the temperature $T = 24$ K predicted from equation (16). The red points and dashed curve and the green squares and dotted curve correspond to other sets of simulations with different perturbation gradients, corresponding to temperatures $T = 707$ K and $T = 3486$ K, respectively. In all cases, the best fits are exponential thus indicating the preserved thermality over a wide range of parameters. Frequency-dependent horizon: (c) Each input frequency in the comoving reference frame experiences a different δn_0 and, consequently a different refractive index gradient (only selected examples from the simulations are shown). (d) Ratio $R = |N|^2/|P|^2$ versus input frequency.

account for dispersion completely. These results, on the one hand, confirm that our analogue model is indeed a good candidate for looking for Hawking-related effects and, on the other, at least partially justifies attempts to describe the analogue model starting from non-dispersive theories and by then extrapolating the behaviour to the dispersive regime.

(ii) The second set of simulations were performed with a varying perturbation velocity and fixed input frequency in the laboratory reference frame. The reason for these simulations lies in the fact that in our experiments the perturbation velocity is varying during propagation. This variation is largest (of the order of 1%) for spontaneous filaments but may also be expected with Bessel filaments due to the self-induced refractive index increase that has the effect of slowing

down the intense peak of the pulse. Although small, this variation is sufficient to introduce a significant frequency dependence of the horizon position that is stronger than that given by dispersion alone. This, in turn, leads to a visible distortion of thermality in the outgoing modes. Figure 5(c) illustrates the changing conditions from one simulation to the next in the comoving reference frame (only four cases are shown as examples): by varying the perturbation velocity, the input frequency slightly changes in the comoving reference frame and experiences the horizon at a different position within the dielectric perturbation, and is thus subject to a different dispersion curve at this horizon. The blue dots indicate the input frequencies on the dispersion curve and the red dots indicate the expected values of the positive ($\omega' > 0$) and negative ($\omega' < 0$) modes. Figure 5(d) shows R as a function of the input frequency in the comoving reference frame. The first four points at higher frequencies do not show any particular variations and we attribute this to a loss of sensitivity as the negative peak falls below the noise floor, which is generated by the input pulse itself (through a process analogous to cross-phase modulation [25]) in the form of a low-intensity spectral pedestal. At lower input frequencies, conversion to the negative mode becomes stronger and may be clearly distinguished (see e.g. figure 4(d)). It may be seen that R follows a linear dependence. This clearly indicates that Hawking mode conversion from our dispersive white hole may not lead to a thermal spectrum. The emitted mode density $\langle \mathcal{N} \rangle = R/(1 - R)$ will exhibit the same values at very high and very low frequencies (where dispersion will be negligible) as in the thermal case, but the absence of an exponential cut-off at blue-shifted frequencies may significantly modify the actual number of photons emitted in the UV region. The relevance of non-thermal emission will be further discussed below.

Summarizing, 1D numerics clearly highlight that the dispersion of our experiments is still sufficiently weak to maintain thermality of the emitted photons. Unfortunately, a thermal emission will not be observed due to the relatively small spectral emission window predicted by equation (13). Moreover, as seen in the second set of numerics, thermality is completely lost in the presence of even very small velocity variations of the perturbation, as in our experiments. These numerical simulations give a clear qualitative prediction of the behaviour of our experiments. However, quantitative predictions may be obtained only by resorting to full 3D + 1 simulations. Indeed, as we will show below, the additional transverse degrees of freedom do play an important role.

8. Photon emission angular distribution

A crucial issue in the experiments described here is the angular distribution of the emitted photons. Based on a dispersionless model in 4D, i.e. the time and full transverse and longitudinal coordinates, albeit with 2D (transversally infinitely extended) dielectric perturbations, we have evaluated that the blackbody emission temperature in the laboratory reference frame is given by [27]

$$T = \frac{1}{\gamma} \frac{1}{1 - \frac{v}{c} n_0 \cos \theta} T_+, \quad (15)$$

where

$$T_+ = \gamma^2 v^2 \frac{\hbar}{2\pi k_B c} \left| \frac{dn}{dx} \right|_{x_H} \quad (16)$$

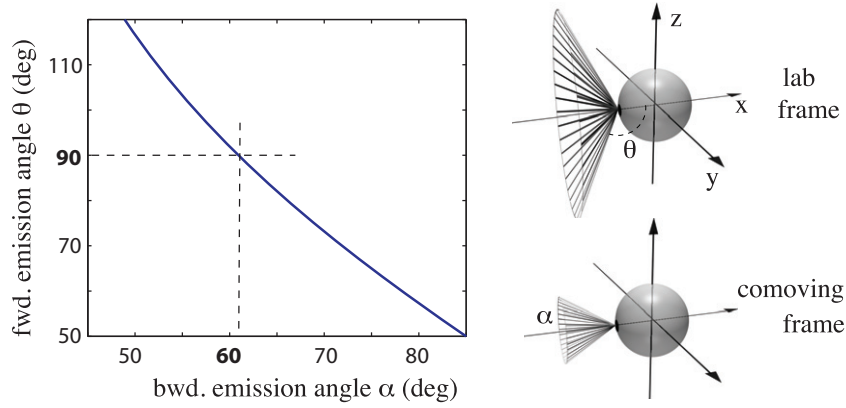


Figure 6. Emission angles in the laboratory reference frame θ versus emission angles in the comoving reference frame, α , measured in the backward direction. The angles are shown in the schematic illustration on the right-hand side. Perturbation velocity $v = 2.065 \times 10^8 \text{ m s}^{-1}$; the central wavelength of the emitted radiation is 850 nm.

is the temperature in the comoving reference frame and θ is the emission angle in the laboratory frame. k_B is the Boltzmann constant and x_H is the position of the horizon. Combined with the fact that typical laser-pulse-induced perturbation shapes will lead to comoving temperatures of the order of 1–30 K, this relation clearly indicates that, whereas an observer in the forward direction ($\theta \sim 0$) will measure temperatures of the order of ~ 2000 K or higher with subsequent emission also in the UV–visible range, observers placed at $\sim 90^\circ$ will observe no photons in the visible spectrum due to the exponential cut-off in the blackbody formula. However, we point out that we have already given both qualitative and quantitative reasons to believe that in our settings the photon emission will not follow a blackbody dependence. This, in turn, implies that there will be no exponential decrease in the photon numbers at high frequencies and photon emission may be more efficient than otherwise expected. It is also worth pointing out that 90° in the laboratory frame correspond to a backward emission in the comoving frame (i.e. in the dielectric black hole frame). Indeed, accounting also for the interface between the FS sample and air, the emission angles in the comoving reference frame, θ' , are related to actually measured angles, θ , in the laboratory reference frame by

$$\cos \theta' = \frac{\cos \theta - \frac{v}{c}}{\sqrt{\left(1 - \frac{v}{c} \cos \theta\right)^2 + (n^2 - 1) \left(1 - \frac{v^2}{c^2}\right)}}. \quad (17)$$

This relation is graphed in figure 6 as a function of the comoving emission angle $\alpha = 180 - \theta'$: a measured angle of 90° corresponds to a backward emission angle of $\sim 55^\circ$ in the comoving frame.

Further information on any off-axis emission is obtained by considering how a seed light pulse (or even a vacuum mode) interacts with a moving perturbation, accounting for the full 3D + 1 geometry. The main novelty introduced by the higher dimensionality (with respect to the 1D + 1 simulations above) is the need to also account for what we may call ‘spatial’ dispersion (in order to distinguish it from the temporal dispersion $n = n(\omega)$ considered so far). In other words, the perturbation will scatter, i.e. reshape, the seed pulse when the two interact. This process has been described in detail in [38]: the seed pulse may be described in terms of its

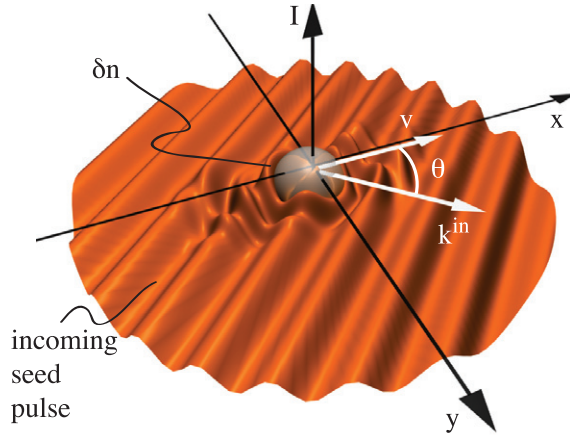


Figure 7. Schematic representation of the interaction geometry between the perturbation (represented as a grey sphere) and a weak seed pulse (in orange).

input and scattered output wave-vector components along the x propagation direction of the perturbation that is moving with velocity v :

$$k_x^{\text{out}} = k_x^{\text{in}} + \frac{\omega^{\text{out}} - \omega^{\text{in}}}{v}. \quad (18)$$

As a first remark, we emphasize that this relation in the laboratory reference frame gives $\omega'_{\text{in}} = \omega'_{\text{out}}$ in the comoving reference frame. In other words, momentum conservation in the laboratory frame is equivalent to energy conservation in the comoving frame and equation (18) describes the scattering process of the input seed into the output positive Hawking mode (see e.g. figure 4(c)). The most remarkable feature of the interaction with the perturbation is that, as shown in [38], the seed pulse is also locally reshaped and exhibits a localized structure that travels locked to the perturbation and at exactly the same group velocity (figure 7).

The formation within the seed pulse of such a peak is a real feature and has been used, for example, to enhance other group velocity-dependent effects by many orders of magnitude, such as stimulated Raman frequency conversion [38, 39]. This process may not be directly likened to the formation of a true group horizon in the standard sense. Nevertheless, in keeping with other experiments, we expect it to lead to an enhancement of the interaction between the IN modes and the perturbation.

Equation (18) also gives some additional insights into the directivity of the emitted photons. In general, the input seed wave may propagate at a generic angle θ_{in} with respect to the perturbation propagation axis, x . Equation (18) may then be written as $k_x^{\text{out}} = |k^{\text{in}}| \cos \theta_{\text{in}} + (\omega^{\text{out}} - \omega^{\text{in}})/v$ and $k_y^{\text{out}} = k_y^{\text{in}} = |k^{\text{in}}| \sin \theta_{\text{in}}$, with y indicating the transverse coordinate. Therefore, the outgoing emission angle in the laboratory frame is

$$\theta_{\text{out}} = \text{atan} \left[\frac{|k^{\text{in}}| \sin \theta_{\text{in}}}{|k^{\text{in}}| \cos \theta_{\text{in}} + (\omega^{\text{out}} - \omega^{\text{in}})/v} \right]. \quad (19)$$

As expected, for $\theta_{\text{in}} = 0$, we also have $\theta_{\text{out}} = 0$, i.e. the Hawking photons are emitted in the forward direction. This is also in keeping with recent studies in a very similar situation in which photon production is predicted within a cone in the forward direction [19]. In the more general case, i.e. for a generic input angle and frequency we see that the outgoing mode angle does not

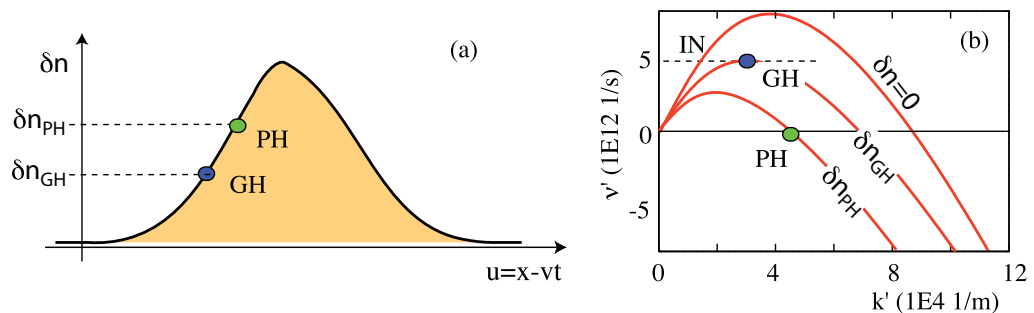


Figure 8. (a) Schematic overview of the horizon positions within the perturbation. (b) Corresponding dispersion curve geometries at two different horizons, as indicated in the figure.

vary significantly with ω^{in} except for very large frequency shifts. Hence, larger emission angles of the order of $\sim 30\text{--}50^\circ$ are to be expected if $\theta_{\text{in}} \gg 0^\circ$ (e.g. $50\text{--}70^\circ$). Such large emission angles may be easily scattered by the medium and we may expect to observe emission at very large angles, $70\text{--}90^\circ$, either directly or from secondary Rayleigh-like scattering that, at these large emission angles, will be very effective.

The qualitative reasoning outlined here suggests that emission may occur at about 90° , either by direct emission at large angles or by secondary scattering of photons from dishomogeneities in the medium. However, a detailed and quantitative estimation of the actual photon numbers generated at each angle requires a yet to be developed full 3D+1 dispersive model.

9. Horizon geometries

Before discussing the experiments, we briefly analyse the existence and features of different kinds of horizons that may appear in analogue models for gravity. We will first introduce the general concepts of phase and group velocity horizons and then discuss in more detail the geometry of the horizon in our settings.

Phase velocity horizons: The phase velocity horizon (PH) is defined as the point within the perturbation at which the phase velocity of a wave is slowed down to zero in the comoving reference frame. The comoving phase velocity is given by $v_\phi = \omega'/k' = \gamma\omega[1 - (v/c)(n(\omega) + \delta n(u))]/k'$, with $u = x - vt$: v_ϕ will therefore be equal to zero for some $\delta n(u) = \delta n_{PH}$, indicated by a green circle (and PH) in figure 8(a). At the phase horizon, only one specific frequency will be blocked.

Group velocity horizons: In the same way, we may define a group velocity horizon (GH), i.e. the point within the perturbation at which the group velocity v_g of a wave is slowed down to zero in the comoving reference frame. In a medium with a subluminal dispersion relation, i.e. such that $v_g < v_\phi$, the group horizon will occur at smaller $\delta n(u) = \delta n_{GH}$ with respect to the phase horizon. This point is indicated with a blue circle (and GH) in figure 8(a). At the group horizon, the incoming pulse will be completely blocked and thus this kind of horizon is also referred to as a ‘blocking horizon’.

Figure 8(b) shows the dispersion relation in the comoving frame: we consider a mode approaching the perturbation (IN mode in the figure). At a generic point outside the perturbation, we have $\delta n = 0$. In order to reach the group horizon, the mode must penetrate further inside the

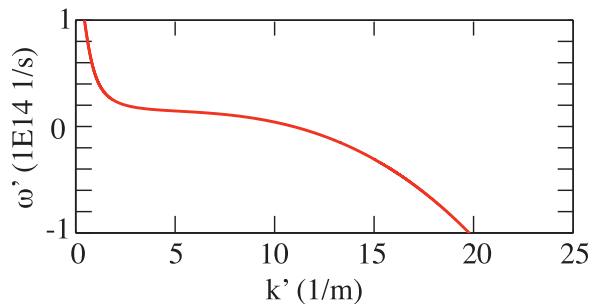


Figure 9. Dispersion relation for FS in the comoving frame of a perturbation generated by a 7° Bessel pulse.

perturbation, δn will thus increase and the dispersion curve will bend further down until the mode comoving frequency passes exactly through the maximum of the dispersion curve, i.e. through the point $v_g = dv'/dk' = 0$. If the phase horizon is to be reached, then the mode would have to penetrate even further in order to reach higher δn values. In general, this will not happen as the pulse will be blocked at the group horizon although one may also envisage a situation in which a group horizon does not exist.

An important observation, derived from the numerical simulation similar to those shown in figure 4, is that the total photon number gain in the two outgoing modes increases sharply as the P- and N-mode frequencies approach the PH condition (data not shown). In the seeded case, the P and N modes may have frequencies that are far from zero with a relatively low amplification gain that is compensated for by the fact that an intense, narrow-band IN mode is injected into the system. However, in the absence of such a narrowband seed pulse, we should consider vacuum fluctuations as a source for seeding the Hawking process: the IN state now has a ‘white’ spectrum and high-gain spectral regions will be favoured over low-gain regions. We may therefore expect spontaneous Hawking emission to produce photons that have frequencies located very close to the PH point, i.e. they will be located within the bandwidth predicted by equation (13). This is the rationale behind the experiments in [1] (also described below) and behind the motivation for claiming that the measured photons are generated at a phase horizon where we imply that it is only the output modes that experience the horizon (and no claim is made regarding the input mode) [1].

It is also generally believed that a group horizon at the *input* frequency is required in order to observe Hawking emission and mode conversion. In figure 9, we show the dispersion relation for FS in the comoving frame of a perturbation generated by a 7° Bessel pulse, as in the experiments described below. The lack of an extremum in this curve implies the absence of a blocking horizon. However, the Sellmeier relations used to derive figure 9 are valid only in a limited frequency range. Bearing in mind that modes generated around $\omega' = 0$ are seeded by very long wavelengths and that the refractive index will decrease beyond the infrared FS resonance ($\sim 10 \mu\text{m}$) we may expect mid- or far-infrared wavelengths to encounter a group horizon and seed Hawking emission.

However, we emphasize that a discussion on the relative role of phase and group horizons is still in progress and a future publication will indeed be devoted to this specific topic.

Horizon geometry: In figure 10, we show the numerically calculated perturbation profile for the (trailing pulse of a) spontaneous filament and indicate the ergosurface (white line) and the qualitative location of the phase horizons (red dotted line). We note that there are two different

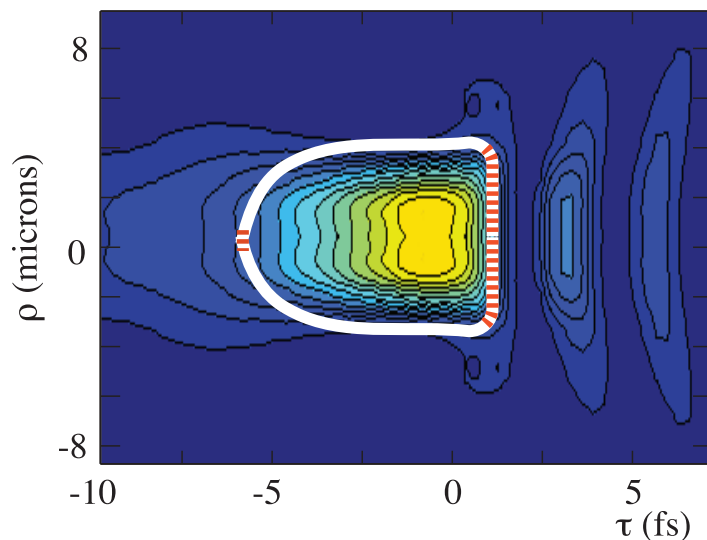


Figure 10. Contour plot of the numerically calculated profile of the perturbation generated by the trailing pulse of a spontaneous filament. The white line indicates the qualitative shape of the ergosurface and the red dotted lines highlight the position of the horizons. The white hole horizon is located on the trailing edge in correspondence to the steep shock front. The black hole horizon is located on the leading edge.

horizons: the leading edge ($\tau < 0$) horizon corresponds to the analogue of a black hole horizon, while the trailing edge ($\tau > 0$) horizon corresponds to the analogue of a white hole horizon. Although in principle both horizons may lead to Hawking emission, it is actually only the white hole horizon that is of true relevance. This is due to two factors: (i) the white hole horizon lies in correspondence to a steep shock front and is therefore expected to give rise to a photon emission that is enhanced by many orders of magnitude with respect to the relatively smooth leading edge of the perturbation.

(ii) While the white hole horizon may actually block incoming light as this is slowed down by the refractive index increase, the black hole horizon will not block light. Consider, for example, light approaching from within the perturbation: if it is travelling slightly faster than v it will catch up with the black hole horizon. However, as it does so, the variation in refractive index red shifts the frequency and dispersion will have the effect of further increasing the light pulse velocity. So the pulse is actually expelled from the perturbation or, in other words, sucked into the region at smaller τ that may be likened to the interior of a black hole. Light therefore interacts only for a very short time with the horizon and this will further reduce any Hawking emission.

10. Experimental layout

The experimental layout is shown in figure 11. The input laser pulse is generated by a regeneratively amplified Nd:glass laser (Twinkle, Light Conversion Ltd, Vilnius, Lithuania). Pulses are delivered with a 10 Hz repetition rate and have 1 ps duration, 1055 nm carrier wavelength, 5 mm diameter at $1/e^2$ and 6 mJ maximum energy. The polarization is kept horizontal for all the measurements shown in this work. Spontaneous filamentation is induced

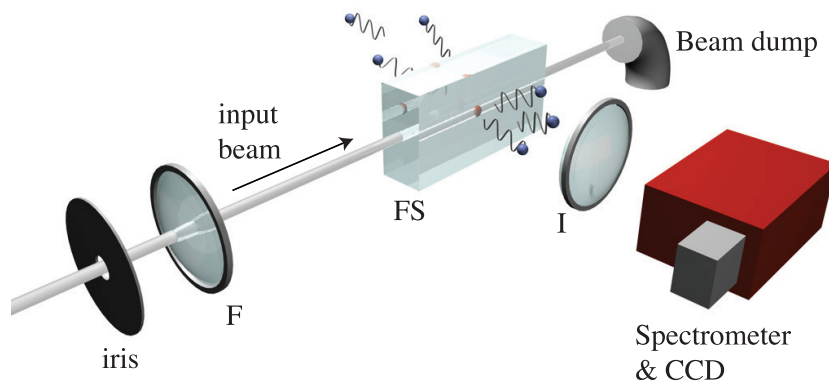


Figure 11. Experimental layout used for detecting analogue Hawking radiation. The horizontally polarized input laser pulse is focused with a 20 cm focal length lens (F) into a sample of FS. The laser pulse undergoes filamentation, reaching extremely high intensities at the nonlinear focus. The position inside the FS sample is controlled using an adjustable iris placed before the focusing lens. The analogue Hawking photons are collected at 90 degrees: an imaging lens (I) collects part of the photons emitted at 90° with respect to the laser pulse direction and sends them to an imaging spectrometer coupled to a cooled CCD camera. The laser pulse at the output of the FS sample is removed by a beam dump.

by loosely focusing the laser pulse with a 20 cm focal length lens into a 2 cm long sample of FS. The position of the point of tightest focus (the nonlinear focus) is controlled by an adjustable iris placed before the focusing lens. The Bessel filament is formed by removing the focusing lens and by placing a conical prism (axicon) directly in front of the FS sample.

The filaments are observed at 90° with respect to the propagation direction by imaging the filament onto the input plane of a spectrometer coupled to a cooled CCD camera. Therefore, in the configuration adopted in these experiments, only those photons emitted at 90° deg with respect to the laser pulse propagation direction are collected.

This choice to collect photons at 90° solves a number of issues. Indeed, it is necessary to distinguish any signature of Hawking radiation from other spurious effects. Specifically, these are

- (i) Rayleigh scattering,
- (ii) spontaneous Raman scattering,
- (iii) self-phase modulation (SPM)-induced spectral broadening or FWM due to the interaction of the intense laser pulse with the Kerr medium,
- (iv) fluorescence from material defects and
- (v) plasma emission.

(i) *Rayleigh scattering* is absent at 90° due to the fact that both the laser pulse and the self-generated supercontinuum signal are horizontally polarized. Spontaneous filaments are known to lead to pulse depolarization when the input power is significantly, e.g. hundreds of times, higher than the threshold power for filamentation. However, we are very far from this condition and typically only a single filament is formed, confirming that we are just above the threshold

power. Moreover, we experimentally measured the filament output polarization and verified that light over the whole spectrum was depolarized by less than 0.1%. This upper limit was actually determined by the polarization-discriminating power of the Glan–Taylor polarizer used for the measurement. Moreover, we may explicitly estimate the expected photon count at 350 nm due to Rayleigh scattering of the depolarized component of the continuum generated by the filament. Less than 1% of the pump pulse is converted into continuum at 350 nm, of which less than 0.1% is depolarized and may be scattered and detected at 90°. Accounting also for the λ^{-4} dependence of Rayleigh scattering we predict a photon count of 1 photon at 350 nm when integrating over 3600 laser pulses. This signal is significantly lower (by 1–2 orders of magnitude) than the photon counts actually measured, and it is attributed to analogue radiation (see below) and may therefore be neglected.

(ii) *Spontaneous Raman scattering* is generated by the pump pulse and results in depolarized emission, in all directions with a spectrum that replicates the pump-pulse spectrum, albeit with a slight red shift [25]. It is precisely this last feature that allows us to easily distinguish Hawking emission from Raman emission: the first is centred at blue-shifted (with respect to the input pump) wavelengths, while the latter is centred around the pump wavelength.

(iii) *Self-phase modulation (SPM)-induced spectral broadening or four-wave mixing (FWM)* are both emitted following well-known laws. SPM is emitted by the filament only in the forward direction and within a tight cone that typically, in FS, has a maximum aperture of 2–3° [20]. FWM must obey energy and momentum conservation conditions, which also constrain the emission to well-defined angles. In particular, no emission is allowed at large angles and is zero around 90° due to the fact that emission at large angles requires a cancellation of the longitudinal momentum of the two pump photons, i.e. the two pump photons must be counter-propagating [25]. In our experiments, the pump pulse is forward propagating and there are no means by which a counter-propagating pulse may be generated (e.g. from a reflection) synchronized with the forward-propagating pump pulse.

Finally, both Rayleigh scattering and nonlinear effects such as FWM or SPM have a well-defined polarization, i.e. in an isotropic medium such as the one we are using, they are expected to bear the same polarization as the input laser pulse. We directly measured the polarization of the emitted photons by placing a polarizer in front of the spectrometer and we found that they are unpolarized. This therefore excludes the possibility of any contribution from coherent, linear or nonlinear scattering effects arising from the pump laser itself.

(iv) *Fluorescence*: All dielectric media exhibit fluorescences of some kind. The choice of the Kerr medium for our experiments is mainly based on the fact that FS is one of the most studied and well-characterized materials available. The fluorescence signal emitted from FS is indeed of significant interest for many applications ranging from telecommunication to deep-UV optics and has therefore been studied under various excitation conditions such as continuous illumination by UV sources, laser excitation in the UV and laser excitation in the infrared. Notwithstanding the numerous fluorescence measurements that may be found in the literature, we note that fluorescence excitation via multi-photon absorption from infrared lasers is somewhat less studied (see e.g. [40, 41]). We therefore experimentally characterized their contribution in order to directly evaluate their importance.

Figure 12(a) shows an example of the output spectrum at 90° over the whole UV to near-infrared range. The different contributions are labelled as follows: *R* for the spontaneous Raman emission that reproduces, as expected, the laser pulse spectrum (with a slight Raman-induced

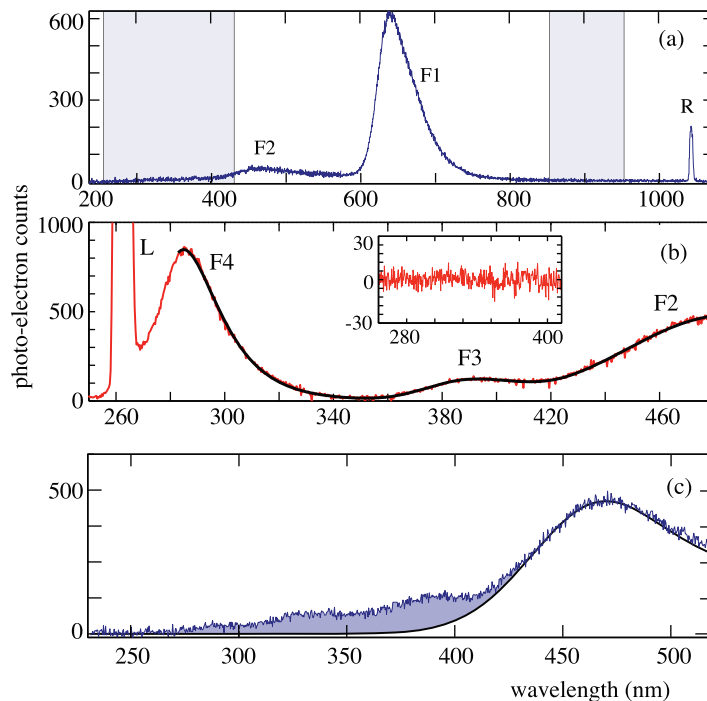


Figure 12. Measurements of fluorescence and analogue Hawking radiation induced by a spontaneous filament. (a) Complete spectrum from the near infrared to the UV showing the main fluorescence peaks. *R* denotes Raman scattering from the pump pulse; F1 and F2 denote fluorescence peaks centred at 650 and 470 nm. (b) Detail of the fluorescence spectrum excited by a 266 nm laser pulse L, showing the presence of two additional peaks, F3 and F4 that are not excited by the infrared laser pulse. The inset shows the remaining signal (0.7 ± 7 counts) after the subtraction of the fluorescence peaks. (c) Measurement of emitted radiation from a spontaneous filament integrated over 3600 laser shots. The shaded region highlights the photoelectron counts that are not ascribable to a fluorescence and are interpreted as analogue Hawking radiation.

red shift); F1 and F2 for the two observed fluorescences. F1 is due to non-bridging oxygen hole centres (NBOHC) and F2 is due to oxygen-deficient centres (ODC). Both of these are first generated by the intense laser pulse and then excited through a photon absorption process (with a 1055 nm pump laser pulse). The F2 fluorescence at 470 nm is particularly due to the cumulative nature of the creation process: non-irradiated areas of the sample show a very weak F2 signal, which steadily increases with irradiation and saturates after ~ 1500 laser shots. A similar behaviour was reported in [40]. The shaded area in figure 12(a) highlights the spectral regions in which we expect (according to the predictions of our model as described above) to observe Hawking radiation from the spontaneous filament (around 350 nm) and from the Bessel filament (around 850 nm). The Bessel filament velocity has been purposely adjusted, by the choice of the cone angle, so that the Hawking spectrum falls in a region free of fluorescence signals. The same holds true for the spontaneous filament; however, additional care should be taken in the UV region, which may exhibit a number of weak fluorescence signals, the details of which depend on the specific concentration of impurities and defects of the FS sample. We therefore further verified the UV fluorescence signals by exciting the medium with a 266 nm laser pulse,

obtained as the fourth harmonic of the 1055 nm laser pulse. Repeating the predictions above for an input 266 nm wavelength, Hawking radiation is expected to be shifted into the deep-UV region (~ 170 nm) and will therefore not be observable due to material absorption and to the limits in the efficiency of the spectrometer and CCD. Conversely, fluorescence signals are known to be optimally excited with 266 nm radiation. Our measurements at 266 nm confirm the fluorescence signals F1 and F2 and, as can be seen in figure 12(b), two new weak fluorescence signals, F3 and F4, also appear.

Therefore, our measurements confirm the results reported in literature and show that only fluorescence peaks F1 and F2 are excited by IR radiation. Since the fluorescence signals are known, they may be subtracted out from any measurements carried out in the same spectral region. In order to do this we first fit the fluorescence signals with a Gaussian function and then subtract the best fit from the measured signal. The black curve in figure 12(b) shows the best fit obtained (in the frequency domain) with Gaussian functions and indeed once this is subtracted out from the measurement, a featureless signal (shown in the inset) is obtained with an average photo-electron count of 0.7 ± 7 . This is a consistency test confirming that the fluorescence signals are all identified and may be consistently subtracted out from any measured spectra. All measurements of analogue Hawking radiation were therefore treated in the same fashion. As an example, in figure 12(c) we show the raw data in the UV region of the emission from a spontaneous filament integrated over 3600 laser shots. The black smooth line shows the Gaussian fit of the fluorescence spectrum and the shaded area highlights the photo-electron counts that are not ascribable to fluorescence and are thus interpreted as analogue Hawking radiation.

(v) *Plasma emission:* We briefly conclude this section by noting that intense laser pulses will generate a plasma in their wake through multiphoton ionization as they propagate through the sample. Density oscillations within this plasma are known to lead to an emission that has been measured and may be used to generate radiation in the THz spectral region. The emission wavelength is centred around the plasma frequency $\omega_p = \sqrt{n_e e^2 / m_e \epsilon_0}$, where n_e , e and m_e are the electron density, charge and mass, respectively [42]. For a relatively high, yet typical for condensed media filaments, the density $n_e = 10^{-19} \text{ cm}^{-3}$ [20], the emission wavelength will therefore be around $\lambda = 9 \mu\text{m}$. This is not only very far away from the measurement range we are interested in here, but also far from the transparency region in FS. Moreover, this emission is emitted within a cone in the forward direction with an angle given by $\alpha \sim \sqrt{\lambda/L}$, where L is the length of the emitting filament [42]. A 1-mm long filament, therefore, gives an emission angle $\alpha \sim 5.4^\circ$ and no emission is expected at 90° .

11. Experimental evidence for analogue Hawking radiation

In this section, we present the experimental data about photon emission from spontaneous and Bessel filaments under the conditions described above. We first show the experimental results obtained from the spontaneous filament.

We measured the spectra around 350 nm, emitted from the dielectric perturbation generated by the spontaneous filament and integrated over 3600 laser shots. The measurements were carried out in sample areas that had not been previously irradiated so as to minimize the contribution from the fluorescence signal centred at 470 nm. Moreover, the fluorescence signal has been fitted with a Gaussian function and subtracted out so as to isolate the spectra shown

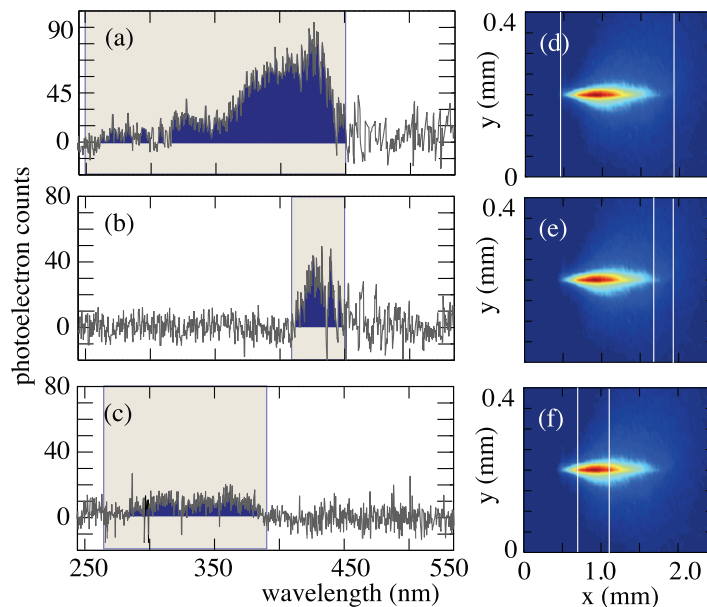


Figure 13. Spectra generated by a spontaneous filament with the pump pulse centred at 1055 nm wavelength. (a)–(c) The spectra when the full filament, the ending or the beginning sections are imaged onto the spectrometer, respectively. The shaded region in (a) shows the predicted emission region. (d)–(f) An image of the filament, as viewed at 90°, and the white lines show the imaged regions.

in figure 13. In particular, figure 13(a) shows the full spectrum obtained by keeping the input slit of the spectrometer fully open in order to collect photons emitted from the whole filament. The filament, imaged at 90°, is shown in figure 13(d) and the white lines indicate the region isolated by the spectrometer slit. The measured spectrum agrees well with the predicted emission region that is indicated by the shaded region in figure 13(a). In figure 14, we show a further measurement carried out with the same experimental setup albeit with a different input laser pulse that had a central wavelength of 800 nm and a duration of 40 fs. Because of the different pulse features, the spontaneous filament dynamics also differ. In particular, the pulse velocities are slightly different and numerical simulations based on the nonlinear Schrödinger equation [20] predict, according to equation (13), a spectral emission window between 270 and 390 nm. As may be seen, the observed photon emission corresponds very well to this prediction. Moreover, we verified that the emitted photons are not polarized.

By placing a broadband polarizer in front of the spectrometer we verified that the photon counts and emission range did not depend on the polarizer angle. Figure 15 shows an example of measurements for two orthogonal orientations of the polarizer. We note that the significantly higher noise in these measurements is due mainly to the 50% loss introduced by the polarizer. The strong reduction in the overall collected light intensity called for much longer integration times (10 min in this case), hence the large noise level. Detection of unpolarized light is expected from a vacuum excitation process and provides further proof that we are not collecting light emitted from coherent phenomena such as FWM or SPM.

Returning to the data in figure 13(a), we note the clear increase in the spectral intensity toward longer wavelengths. We attribute this to the fact that the perturbation velocity is varying along the filament length with a non-uniform acceleration (see figure 2(b)), resulting in larger

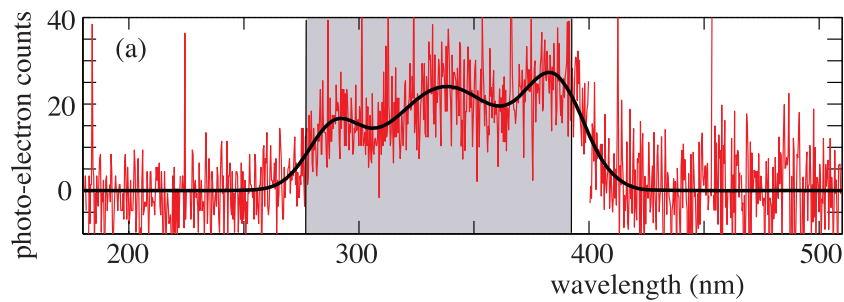


Figure 14. Spectrum generated by a spontaneous filament with a pump-pulse central wavelength of 800 nm. The shaded area highlights the predicted emission range.

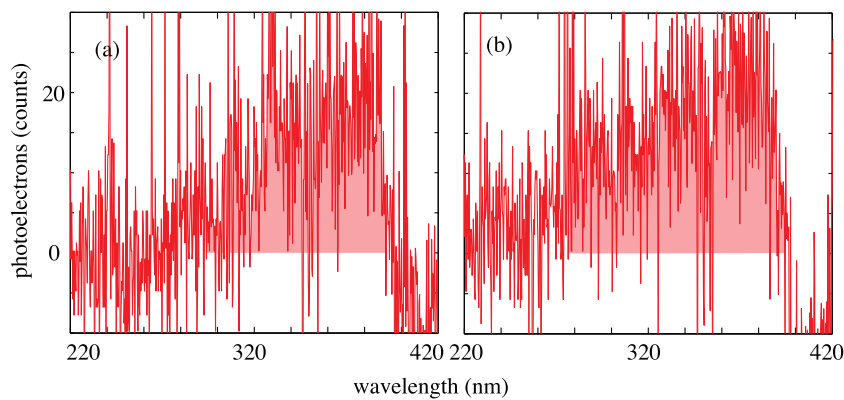


Figure 15. Spectrum generated by a spontaneous filament with a pump-pulse central wavelength of 800 nm. Both (a) and (b) were taken under identical measurement conditions after placing a broadband polarizer in front of the spectrometer. The two graphs show measurements for orthogonal orientations of the polarizer, i.e. of the measured photons.

accumulation of photons for smaller variations of the velocity, i.e. towards the end of the filament. According to equation (13), this should result in the accumulation of photons at longer wavelengths.

We verified this interpretation by closing the spectrometer input slit so as to select different longitudinal portions of the filament. Figures 13(b) and (c) show the spectra emitted from the beginning and final sections of the filament, respectively, highlighting how the emitted spectrum shifts in agreement with predictions. In the final section of the filament, the blue part of the spectrum is completely missing, and vice versa, in the beginning section of the filament, only the blue part is visible and longer wavelengths are completely suppressed.

The fact that the spectrum changes in such a dramatic way by simply changing the position along the filament at which it is collected is a completely new observation and, to the best of our knowledge, does not find an explanation in any standard (e.g. four wave mixing of self-phase modulation) mechanism. This finding indicates that the filament is exciting a 90° emission of photons whose wavelength depends on some specific feature of the filament that is changing along the propagation direction. An obvious conclusion in the context of the model presented above is that this specific feature is the pulse velocity as predicted by equation (13). Indeed,

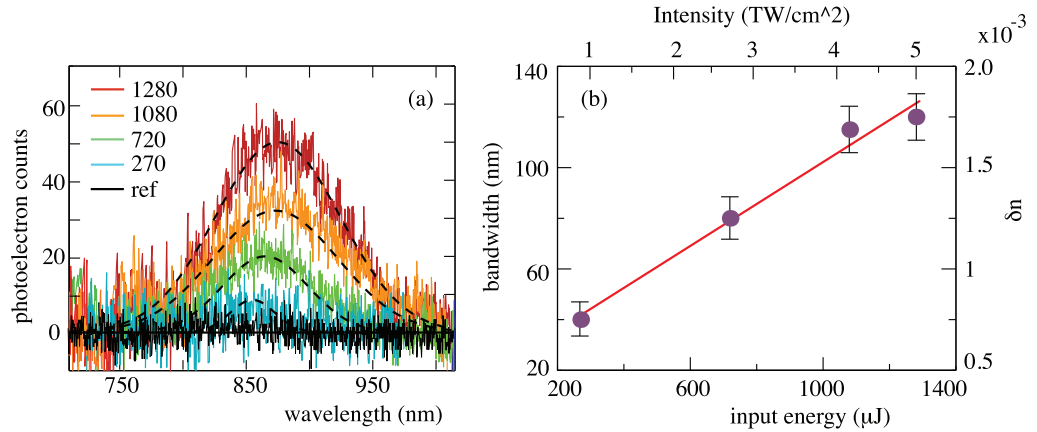


Figure 16. (a) Spectra generated by a Bessel filament. Five different curves are shown corresponding to a reference spectrum obtained with a Gaussian pulse (black line) and four different input Bessel energies: 1280, 1080, 720 and 270 μJ . Dashed lines are a guide to the eye. (b) Dielectric perturbation δn derived from the measured bandwidths in (a) versus the input energy and intensity. The solid line shows the best linear fit $\delta n = n_2 I$ with slope $n_2 = 2.8 \pm 0.5 \times 10^{-16} \text{ cm}^2 \text{ W}^{-1}$.

both the velocity profile (i.e. lower/higher velocities in the first/last section of the filament) and the absolute values of the velocities are in good agreement with the measured spectra according to our model of analogue Hawking emission. We thus interpret the observed spectra as evidence of a Hawking-like photon emission.

We now consider the Bessel filament. For sufficiently large Bessel cone angles, θ , the filament does not exhibit spontaneous dynamics and the velocity is constant and is given by $v = v_G / \cos \theta$ [23]. The Bessel cone angle is chosen so as to place the Hawking spectrum away from any material fluorescences. Indeed, for $\theta = 7^\circ$, the spectrum is predicted to be in the 850–950 nm range, which, as can be seen in figure 12(a), does not coincide with any known or measured fluorescence in FS.

We note that the Bessel filament represents in a certain sense the ideal experimental situation: the perturbation velocity is constant and the laser pulse is no longer affected by intensity clamping so that we may vary the amplitude of the dielectric perturbation. Therefore the emitted bandwidth will depend only on $\delta n = n_2 I$, which may be controlled by varying the input pulse energy.

The black line in figure 16(a) shows a reference spectrum obtained from the spontaneous filament. There are no peaks in this spectrum that shows only noise, thus underlining the absence of any fluorescence or other possible emission signals when the perturbation v does not satisfy equation (13). The other four curves show the emitted spectra for four different input energies of the Bessel filament, as indicated in the figure. These measurements show that the bandwidth of the emission is clearly increasing with the input energy (the dashed lines are Gaussian fits to the spectra).

The filament intensity is a known function of the input energy and the measured bandwidth may be used to estimate δn using equation (13). In figure 16(b), we show these results: the solid line shows a linear fit $\delta n = n_2 I$ whose slope is $n_2 = 2.8 \pm 0.5 \times 10^{-16} \text{ cm}^2 \text{ W}^{-1}$. This value is very close to the tabulated value of $n_2 \sim 3 \times 10^{-16} \text{ cm}^2 \text{ W}^{-1}$ [20, 29], thus showing that there

is agreement also at the quantitative level between the measurements and the model based on Hawking emission.

Finally, we note that the maximum emission peaks in figure 16(a) show a 40 nm red shift with increasing input energy. This is explained as a result of the fact that equation (13) predicts that as the perturbation amplitude δn is increased, only the left-hand side of the relation is changed: for increasing δn , the red-wavelength edge of the emission window will shift to redder wavelengths. Using the data of the experiment, equation (13) predicts a shift of the emission centre by a total of 45 nm, which is in very good agreement with what we actually observe.

Overall, our measurements of photon emission at 90° from filaments, under different conditions, show a number of features that have never been observed so far and that do not find an explanation in terms of typical nonlinear optical processes. These features are

- (i) a clear emission in spectral regions that depend on the pump-pulse velocity,
- (ii) a spectral emission bandwidth that varies linearly with the value of the Kerr-induced perturbation, and
- (iii) a spectral emission peak that varies with the input energy. We have shown how these features are in both qualitative and quantitative agreement with the predictions of the Hawking model presented above and summarized in the simple relation, equation (13).

12. Concluding remarks

We have presented experimental results on the excitation of photons by means of a refractive index perturbation that travels at the same velocity as that of the excited emission. The dielectric perturbation is generated by an intense laser pulse that interacts with the medium through the nonlinear Kerr index. However, it is important to note that the excitation mechanism is not essential for the observation of the photon emission: the necessary ingredient is the perturbation itself and not the method used to generate it.

The observed photon emission bears a series of very peculiar features that are hard to explain on the basis of any known optical processes. Conversely, a model based on an analogue of Hawking radiation, adapted to account for the peculiarities of the experimental setting, is able to capture the salient characteristics highlighted in this work.

There remain a number of issues to be studied and elaborated. At the current state of the art, we are not able to provide an accurate description of the angular emission that, in particular, properly accounts for the relatively strong emission at 90° . A full dimensional model that accounts for the actual geometry of the filament and full material dispersion is lacking and would possibly give the missing quantitative evaluation for the angular distribution of the emitted photons. Detection of correlations between photon pairs is also an important issue that, however, could also be tackled in a somewhat different geometry, e.g. in optical fibres as originally suggested by Philbin *et al* [9], such that the emitted photons are constrained along the same propagation direction. A further topic that is closely related to that of Hawking emission is the so-called mode conversion whereby an input photon is converted into a positive and a negative frequency (in the comoving reference frame) photon. Mode conversion may be studied by attempting to seed the analogue horizon with a classical seed pulse, similarly to what has been done with gravity waves in water [33, 34]. Our experiments thus indicate that an important quantity for *predicting* the emission spectrum in our settings is indeed the *phase* velocity horizon. Moreover, it was pointed out in [1] that in the Bessel filament experiments there are no

frequencies relatively close to the input laser frequency which may experience a group horizon. At sufficiently large frequency shifts the dispersion curve is such that a maximum, i.e. the point at which the comoving group velocity goes to zero, naturally occurs. Nevertheless, we also have preliminary indications, from numerical simulations similar to those described in this work, that the group horizon is not essential for Hawking mode conversion. Future work will be devoted specifically to this topic. Indeed, a detailed analysis of the relative role of group and phase horizons with varying dispersion relations, e.g. such as to create only one or the other kind of horizon, is currently lacking.

A further intriguing issue that needs to be addressed is the influence of vacuum squeezing on the Hawking radiation intensity. Indeed, it has been recently pointed out that a properly prepared vacuum state can increase the emissivity by many orders of magnitude [43]. These findings are relevant to our measurements, because cross-phase modulation induced by an intense pump will squeeze the vacuum. This has been experimentally verified in fibre geometries [44] and has also been predicted to occur in settings identical to those used in these experiments, whereby a progressive undistorted squeezed vacuum state is generated [45]. Typical values of the squeezing obtained in experiments correspond to the creation of ~ 1 photon per pulse [44] that may then seed Hawking emission. According to [43], this is already sufficient to lower the required temperature (or equivalent surface gravity) for observing Hawking radiation by 4–6 orders of magnitude. This process must therefore be properly accounted for in future models attempting to give quantitative estimations of the emission photon numbers. In conclusion, Hawking radiation was predicted many years ago in an astrophysical context and was then predicted to be characteristic of a wide range of physical settings. However, it is an extremely elusive phenomenon and even certain basic features of the effect such as mode conversion are still not fully understood. We believe that the dielectric analogue proposed for the first time by Philbin *et al* and the measurements presented in this paper represent a significant step forward in the experimental investigation of Hawking and Hawking-related effects.

Acknowledgments

We acknowledge P Di Trapani and A Couairon for technical assistance at the Virtual Institute of Nonlinear Optics (VINO) and the VINO numerical laboratory. Discussions with U Leonhardt, I Carusotto, G Adesso and I Fuentes are also gratefully acknowledged.

References

- [1] Belgiorno F, Cacciatori S L, Clerici M, Gorini V, Ortenzi G, Rizzi L, Rubino E, Sala V G and Faccio D 2010 Hawking radiation from ultrashort laser pulse filaments *Phys. Rev. Lett.* **105** 203901
- [2] Leonhardt U and Philbin T G 2009 Transformation optics and the geometry of light *Prog. Opt.* **53** 69–152
- [3] Leonhardt U 2006 Optical conformal mapping *Science* **312** 1777
- [4] Leonhardt U and Tyc T 2009 Broadband invisibility by non-Euclidean cloaking *Science* **323** 110
- [5] Roberts D A, Kundtz N and Smith D R 2009 Optical lens compression via transformation optics *Opt. Express* **17** 16535–42
- [6] Ginis V, Tassin P, Craps B and Veretennicoff I 2010 Frequency converter implementing an optical analogue of the cosmological redshift *Opt. Express* **18** 5350–5
- [7] Schützhold R 2009 Recreating fundamental effects in the laboratory? *Adv. Sci. Lett.* **2** 121–32

- [8] De Lorenzi V A, Klippert R and Yu. Obukhov N 2003 Optical black holes in moving dielectrics *Phys. Rev. D* **68** 061502
- [9] Philbin T G, Kuklewicz C, Robertson S, Hill S, Konig F and Leonhardt U 2008 Fiber-optical analog of the event horizon *Science* **319** 1367
- [10] Faccio D, Cacciatori S, Gorini V, Sala V G, Averchi A, Lotti A, Kolesik M and Moloney J V 2010 Analogue gravity and ultrashort laser pulse filamentation *Europhys. Lett.* **89** 34004
- [11] Barceló C, Liberati S and Visser M 2005 Analogue gravity *Living Rev. Relativ.* **8**
- [12] Birrell N D and Davies P C W 1982 *Quantum Fields in Curved Space* (Cambridge: Cambridge University Press)
- [13] Novello M, Visser M and Volovik G E 2002 *Artificial Black Holes* (Singapore: World Scientific)
- [14] Hawking S W 1974 Black hole explosions? *Nature* **248** 30–1
- [15] Hawking S 1975 Particle production by black holes *Commun. Math. Phys.* **43** 199–220
- [16] Unruh W G 1981 Experimental black-hole evaporation? *Phys. Rev. Lett.* **46** 1351–3
- [17] Balbinot R, Fabbri A, Fagnocchi S, Recati A and Carusotto I 2008 Nonlocal density correlations as a signature of Hawking radiation from acoustic black holes *Phys. Rev. A* **78** 021603
- [18] Carusotto I, Fagnocchi S, Recati A, Balbinot R and Fabbri A 2008 Numerical observation of Hawking radiation from acoustic black holes in atomic Bose–Einstein condensates *New J. Phys.* **10** 103001
- [19] Guerreiro A, Ferreira A and Mendonça J T 2001 Production of bright entangled photons from moving optical boundaries *Phys. Rev. A* **63** 052302
- [20] Couairon A and Mysyrowicz A 2007 Femtosecond filamentation in transparent media *Phys. Rep.* **441** 47–189
- [21] Bergé L, Skupin S, Nuter R, Kasparian J and Wolf J P 2007 Ultrashort filaments of light in weakly ionized, optically transparent media *Rep. Prog. Phys.* **70** 1633–713
- [22] Polesana P, Couairon A, Faccio D, Parola A, Porras M A, Dubietis A, Piskarskas A and Di Trapani P 2007 Observation of conical waves in focusing, dispersive, and dissipative Kerr media *Phys. Rev. Lett.* **99** 223902
- [23] Polesana P, Dubietis A, Porras M A, Kučinskas E, Faccio D, Couairon A and Di Trapani P 2006 Near-field dynamics of ultrashort pulsed Bessel beams in media with Kerr nonlinearity *Phys. Rev. E* **73** 56612
- [24] Friberg A T 1996 Stationary-phase analysis of generalized axicons *J. Opt. Soc. A* **13** 743
- [25] Boyd R 2008 *Nonlinear Optics* 3rd edn (New York: Academic)
- [26] Cacciatori S L, Belgiorno F, Gorini V, Ortenzi G, Rizzi L, Sala V G and Faccio D 2010 Spacetime geometries and light trapping in travelling refractive index perturbations *New J. Phys.* **12** 095021
- [27] Belgiorno F, Cacciatori S L, Ortenzi G, Rizzi L, Gorini V and Faccio D 2011 Dielectric black holes induced by a refractive index perturbation and the Hawking effect *Phys. Rev. D* **83** 024015
- [28] Jacobson A T and Kang G 1993 Conformal invariance of black hole temperature *Class. Quantum Grav.* **10** L201–6
- [29] De Salvo R, Said A A, Hagan D J, Van Stryland E W and Sheik-Bahae M 1996 Infrared to ultraviolet measurements of two-photon absorption and n_2 in wide bandgap solids *IEEE J. Quantum Electron.* **32** 1324–33
- [30] Ginzburg V L and Frolov V P 1987 Vacuum in a homogeneous gravitational field and excitation of a uniformly accelerated detector *Sov. Phys.—Usp.* **30** 1073
- [31] Unruh W G 1995 Sonic analog of black holes and the effects of high frequencies on black hole evaporation *Phys. Rev. D* **51** 2827
- [32] Corley S and Jacobson T 1996 Hawking spectrum and high frequency dispersion *Phys. Rev. D* **54** 1568
- [33] Rousseaux G, Mathis C, Maïssa P, Philbin T G and Leonhardt U 2008 Observation of negative-frequency waves in a water tank: a classical analogue to the Hawking effect *New J. Phys.* **10** 053015
- [34] Weinfurter S, Tedford E W, Penrice M C J, Unruh W G and Lawrence G A 2011 Measurement of stimulated Hawking emission in an analogue system *Phys. Rev. Lett.* **106** 021302
- [35] Macher J and Parentani R 2009 Black/white hole radiation from dispersive theories *Phys. Rev. D* **79** 124008
- [36] Mayoral A, Recati A, Fabbri A, Parentani R, Balbinot R and Carusotto I 2010 Acoustic white holes in flowing atomic Bose–Einstein condensates arXiv:1009.6196

- [37] Yee K 1966 Numerical solution of initial boundary value problems involving Maxwell's equations in isotropic media *IEEE Trans. Antennas Prop.* **14** 302
- [38] Faccio D, Averchi A, Couairon A, Kolesik M, Moloney J V, Dubietis A, Tamosauskas G, Polesana P, Piskarskas A and Di Trapani P 2007 Spatio-temporal reshaping and X wave dynamics in optical filaments *Opt. Express* **15** 13077–95
- [39] Faccio D, Averchi A, Dubietis A, Polesana P, Piskarskas A, Di Trapani P and Couairon A 2007 Stimulated raman X waves in ultrashort optical pulse filamentation *Opt. Lett.* **32** 184–6
- [40] Zoubir A, Rivero C, Grodsky R, Richardson K, Richardson M, Cardinal T and Couzi M 2006 Laser-induced defects in fused silica by femtosecond IR irradiation *Phys. Rev. B* **73** 224117
- [41] Skuja L 1998 Optically active oxygen-deficiency-related centers in amorphous silicon dioxide *J. Non-Cryst. Solids* **239** 16–48
- [42] Amico C D, Houard A, Akturk S, Liu Y, Le Bloas J, Franco M, Prade B, Tichonchuk V T and Mysyrowicz A 2008 Forward THz radiation emission by femtosecond filamentation in gases: theory and experiment *New. J. Phys.* **10** 013015
- [43] Aspachs M, Adesso G and Fuentes I 2011 Optimal quantum estimation of the Unruh–Hawking effect *Phys. Rev. Lett.* **105** 151301
- [44] Margalit M, Yu C X, Ippen E P and Haus H A 1988 Cross phase modulation squeezing in optical fibers *Opt. Express* **2** 72
- [45] Ciattoni A and Conti C 2007 Quantum electromagnetic X waves *J. Opt. Soc. B* **24** 2195